Radiation Effects
1973, Vol. 20, pp. 1–24

© Gordon and Breach Science Publishers Ltd.
Printed in Great Britain

Review Article

BETWEEN WAVE AND PARTICLE–THE SEMICLASSICAL METHOD FOR INTERPRETING HIGH-ENERGY ELECTRON MICROGRAPHS OF CRYSTALS

M. V. BERRY, B. F. BUXTON and A. M. OZORIO DE ALMEIDA

H. H. Wills Physics Laboratory, Tyndall Avenue, Bristol BS8 1TL, U.K.

(Received May 7, 1973)

The concepts of "semiclassical mechanics" are applied to the propagation of an electron beam through a crystal lattice. We obtain a variety of approximate descriptions which bridge the gap between the full quantum treatment necessary at lower voltages and the purely classical analysis which becomes valid at higher voltages. These methods, which are all based on "real space", lead to simple physical descriptions and numerically accurate formulae for phenomena which have previously only emerged after lengthy computations based on Fourier analysis: examples are the existence of "critical voltages" and "critical angles". It is shown how the purely classical concept of "caustic" can explain features on micrographs which are usually considered as interference fringes; this bypasses the need to construct "dispersion surfaces". Absorption from the diffracted beams, which is caused by inelastic scattering, is incorporated into the semiclassical analysis.

1 INTRODUCTION–THE NATURE OF EXPERIMENTS AND BASIC THEORETICAL MODEL

It has been appreciated for some time[1,2] that high-voltage electron microscopy operates in the transition regime between the quantum and classical descriptions of electron propagation. Thus the firmly quantum-mechanical formalism developed originally for x-ray diffraction, in which the crystal potential is expanded in a Fourier series and Schrödinger's equation solved by matrix diagonalization,[3] either converges too slowly when applied to high-energy electrons, or else results in computations which are not easy to interpret. On the other hand, the purely classical analysis[4] developed for heavy-particle channelling takes no account of the interference processes which manifestly occur with electrons. To provide a conceptual framework for understanding micrographs taken in the transition range, an analytical theory (Ref. 5, hereafter called I) was devised, starting from Schrödinger's equation and arriving at the classical limit after a series of approximations which become valid as the voltage increases. This multi-stage nature of the passage to the classical limit was the main result of I; it means that at a given energy some observations on a crystal may be interpreted classically, while others may not.

In this article we aim to review the ideas introduced in I in a form accessible to readers with no interest in the intricate details of the underlying mathematics, and to show how semiclassical concepts provide simple interpretations for a wide range of observations. We shall proceed in the reverse direction to I, beginning with the purely classical case and gradually penetrating the subtleties of the wave theory which are required as the voltage is reduced. We shall employ a recent review[6] (hereafter called II) as a standard reference source for concepts and techniques generally used in semiclassical theory.

We shall be concerned with microscope images formed by *diffraction contrast*. What this means is

---

ABOUT THE AUTHORS

Dr. M. V. Berry is a graduate of the universities of Exeter and St. Andrews and is a lecturer in the department of physics at the university of Bristol. He is author of the book *The Diffraction of Light by Ultrasound* but his interests range widely from interpretations of the concept of surface tension to echo sounding in glaciers. He is especially interested, however, in all problems associated with wave/particle duality and the use of semiclassical approximations in wave mechanics.

Mr. A. M. Ozorio de Almeida and Mr. B. F. Buxton are colleagues of Dr. Berry, collaborating with him on the particular problem of application of semiclassical methods and concepts to high energy electron diffraction and microscopy, and to channelling.

illustrated schematically in Figure 1. A parallel beam of electrons with wave vector $\mathbf{k}_0$ is incident on a crystalline specimen of thickness z whose entrance face lies in the "horizontal" plane (if the crystal is bent, this defines a local horizontal). After propagating

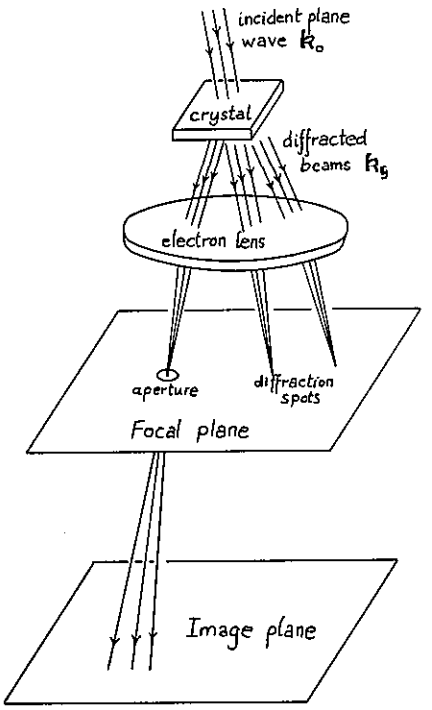

FIGURE 1 Arrangement for diffraction contrast microscopy (schematic).

through the crystal the electron beam emerges at the exit face, where its wave function forms the "object" which is imaged by the microscope. Because the crystal is a periodic structure, the elastically transmitted waves form a series of diffracted beams travelling in directions $\mathbf{k}_G$, whose horizontal components are

$$\mathbf{K}_G = \mathbf{K}_0 + \mathbf{G}, \tag{1.1}$$

$\mathbf{K}_0$ being the horizontal component of $\mathbf{k}_0$ and $\mathbf{G}$ being the set of crystal reciprocal lattice vectors in the horizontal plane (see I, Section 2). These diffracted beams are focussed by a lens. What we see depends on where we look: in the *focal plane* each beam is brought separately to a focus, and we see a pattern of spots—the "diffraction pattern". If the amplitude of the Gth beam is $A_G(z, \mathbf{K}_0)$, then the brightness of the Gth diffraction spot is proportional to $|A_G|^2$. In the *image plane* we see a real-space image of the wave function at the exit face of the crystal.

In diffraction contrast microscopy only one diffracted beam is allowed past the focal plane (via an aperture) to form the image. If this is the undeviated beam ($\mathbf{G} = 0$), a "bright-field" image is produced, while any other beam ($\mathbf{G} \neq 0$), produces a "dark-field" image. The beauty of this technique is that only *elastically diffracted* electrons need be considered, provided absorption is included in a manner explained in Section 6. Obviously, these diffraction contrast images will be of uniform brightness if the specimen is perfectly flat with parallel faces. But if the crystal is buckled, or if its thickness varies, then the brightness will not be uniform, because the intensity $|A_G(z, \mathbf{K}_0)|^2$ at a given image point, when the Gth diffracted beam is employed, depends on the local thickness z and orientation $\mathbf{K}_0$ at the corresponding object point. Thus lines on the image are "bend contours" or "thickness fringes" joining points of constant $|A_G(z, \mathbf{K}_0)|^2$ for fixed $\mathbf{G}$. In the absence of defects (which are readily identifiable) these diffraction contrast images depend sensitively on the crystal potential $V(\mathbf{r})$ which acts on the electron beam, so that this type of microscopy, using deliberately bent specimens, is a powerful source of information about the fine structure of crystalline matter. The contrast arises from the cooperative effect of very many atoms in each region where z and $\mathbf{K}_0$ are almost constant, so that the image brightness varies slowly over many crystal lattice spacings. (On the other hand, ordinary images, formed with all the emergent electrons, can under suitable conditions resolve single lines of atoms; but inelastic scattering is involved, and no accurate measurement of the crystal potential has been made by this direct method.)

The electron wavelength λ is very small, being given as a function of its kinetic energy E by the relativistic formula

$$\lambda = \frac{2\pi}{|\mathbf{k}_0|} = \frac{h}{(2m_0E)^{1/2}(1 + E/2m_0c^2)}, \tag{1.2}$$

where m_0 is the electron rest mass ($m_0c^2 = 511$ kV) and h is Planck's constant. When E is 1 MeV, λ is 0.0087 Å. Such wavelengths are far smaller than a typical lattice spacing a, so that the angular separation between neighbouring diffracted beams, which is given by twice the Bragg angle θ_B, where

$$\theta_B = \lambda/2a, \tag{1.3}$$

is extremely small—frequently much less than a degree. If the energy is extremely high, θ_B is so small that the diffracted beams cannot be resolved, and a fan of radiation is observed continuously distributed over a range of scattering angles near the forward direction. In these cases diffraction contrast observations cannot be made

(the practical difficulties that limit resolution are keeping the incident beam collimated within θ_B, and making an aperture small enough to let through just one diffracted beam).

Where diffraction contrast is possible, the principal theoretical problems are to calculate the image intensity $|A_G(z, \mathbf{K}_0)|^2$ as a function of $\mathbf{G}$, z, $\mathbf{K}_0$ and the energy E, and to devise ways of inferring the crystal potential $V(\mathbf{r})$ from measurements on the image. In general these are formidable three-dimensional wave propagation problems, but in the high-energy régime a basic simplification is possible: it is shown in Section 2 of I that for high-energy scattering the potential $V(\mathbf{r})$ may be replaced by its average value, taken over a distance of several lattice spacings along the direction $\mathbf{k}_0$ of the incident electrons. This basic result is valid whether the particles propagate classically[4] or quantum-mechanically,[3] and arises because the important scattering at high energies occurs near the forward direction. We denote the reduced "projected potential" by $\bar{U}(\mathbf{r})$, defined by

$$\bar{U}(\mathbf{r}) \equiv \frac{2m(E)}{\hbar^2 l} \int_{-l/2}^{l/2} \mathrm{d}s V(\mathbf{r} + s\mathbf{k}_0/k). \qquad (1.4)$$

k is simply $2\pi/\lambda$, $m(E)$ is the relativistic mass, given by

$$m(E) = m_0 + E/c^2, \qquad (1.5)$$

and l is an averaging distance whose value is typically several lattice spacings. Thus $\bar{U}(\mathbf{r})$ increases with energy, and this fact is responsible for the gradual onset of "classicality", as we shall see. We therefore have a quantum problem which may be treated classically at high energies because of a relativistic effect!

If $\mathbf{k}_0$ is not almost parallel to a principal plane of atoms in the crystal, $\bar{U}(\mathbf{r})$ is almost independent of r, so that the specimen acts like a homogeneous medium and no diffraction or channelling occurs. The interesting situations occur when $\mathbf{k}_0$ is nearly parallel to a principal atomic plane; then two special cases are important:

i) *k_0 almost parallel to a plane but not to a line of atoms in the plane.* It is easily seen from (1.4) that $\bar{U}(\mathbf{r})$ then only depends on a single coordinate x which varies perpendicular to the planes, and the crystal is effectively one-dimensional giving rise to a single row of diffraction spots. This is the case of "systematic diffraction", which corresponds to the "planar channelling" of heavy particles. The potential $\bar{U}(x)$ is often of the form shown schematically in Figure 2; for later convenience we have made the zero values of x and U correspond with the top of a potential barrier between "averaged planes" of atoms. The cusps

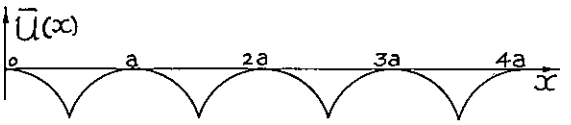

FIGURE 2 One-dimensional potential for "systematic" diffraction.

between the atomic planes are the result of projecting the Coulomb cores of the atoms; one effect of thermal vibrations (Section 6) is to smooth away these cusps, over a distance of about $a/10$. In diffraction contrast microscopy a bent wedge of crystal (Figure 3) is

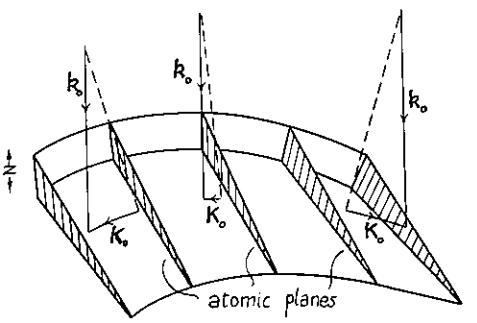

FIGURE 3 Bent wedge specimen for "systematic" diffraction.

employed to study scattering from planes, so that K_0 (i.e. the x component of $\mathbf{K}_0$) and z vary across the specimen; thus the image intensity is a direct map of $|A_G(z, K_0)|^2$ as a function of K_0 and z.

ii) *k_0 nearly parallel to a line of atoms.* In this case $\bar{U}(\mathbf{r})$ depends only on a two-dimensional coordinate $\mathbf{R} = (x, y)$ perpendicular to the lines or "strings"[4] of atoms. This is the case of "cross-grating diffraction", which corresponds to the "axial channelling" of heavy particles. The Coulomb cores of the atoms, when projected, give logarithmic singularities in $\bar{U}(\mathbf{R})$ at the atomic strings, instead of the cusps of Figure 2, but these too are smoothed out by thermal vibrations. In experiments on this case a dome-shaped specimen (Figure 4) of constant thickness is employed; thus the image intensity is a direct map of $|A_G(z, \mathbf{K}_0)|^2$ as a function of K_{0x} and K_{0y}.

Thus the basic theoretical model is of electrons propagating elastically in one- or two-dimensional structures made up of planes or strings of atoms which are projections of the actual three-dimensional crystal. The precise nature of the propagation, in particular the degree to which it can be described classically, will be explored in the remaining sections of this article. Although we shall find (Sections 2–4) that many observations can be explained "almost classically",

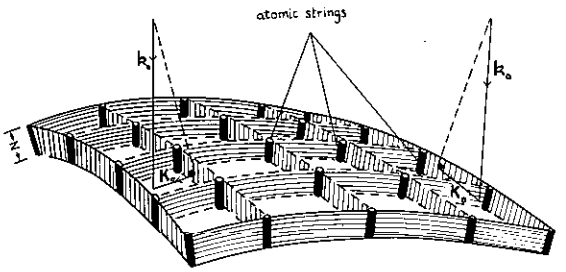

FIGURE 4 Dome-shaped specimen for "cross-grating" diffraction.

our methods also deal accurately with typically "wave" effects associated with the Bloch eigenvalues and eigenfunctions (Sections 5–7). The type of semi-classical analysis employed here was designed especially to work out the detailed consequences of elastic propagation among strings or planes; to study the quantal effects associated with the breakdown of this model, a different analysis[4a] might be needed.

2 INTERFERING CLASSICAL PATHS–PHASE, AMPLITUDE, CAUSTICS

On this most primitive propagation model, electrons are assumed to travel through the crystal along classical paths, winding their way through the lattice of strings or planes under the influence of the projected potential $\bar{U}(\mathbf{R})$. Each path makes a complex contribution to the total wave function, the *amplitude* being proportional to the square root of the local density of paths, and the *phase* being equal to the *classical action function* for the path, divided by $\hbar$ (see Section 7 of II). It is essential to understand precisely which family of classical paths is involved; this will be explained using Figure 5, which is drawn for the more general two-dimensional case. The initial conditions define an ensemble of particles all with momentum $\hbar\mathbf{k}_0$, which strike the specimen at positions $\mathbf{R}_0(= x_0, y_0)$ distributed uniformly over its entrance face. The particles travel along classical paths, and emerge from the crystal at positions $\mathbf{R}$ with momenta $\hbar\mathbf{k}$, both quantities being functions of $\mathbf{K}_0$, $\mathbf{R}_0$ and the thickness z. Because of the lattice structure of the specimen the pattern of paths will be periodic in $\mathbf{R}$ and $\mathbf{R}_0$, and it is easily seen that any path emerging in a direction $\mathbf{K}$ not equal to one of the $\mathbf{K}_G$ defined by (1.1) will give zero contribution because of destructive interference with its counterparts from other unit cells of $\bar{U}(\mathbf{R})$.

Therefore the amplitude $A_G(z, \mathbf{K}_0)$ of the Gth diffracted beam contains contributions only from those paths which emerge with horizontal momenta

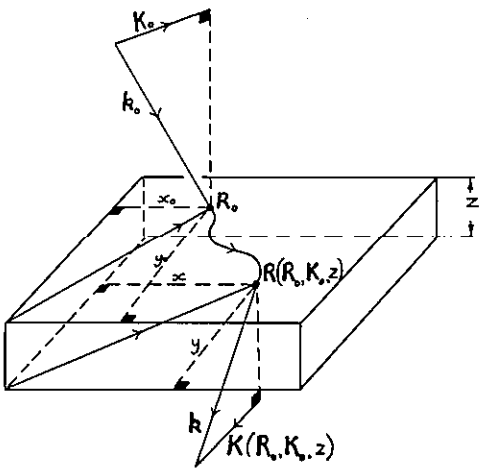

FIGURE 5 Notation for classical paths.

$\hbar\mathbf{K}_G$. These paths were incident at z = 0 at isolated points $\mathbf{R}_0{}^i(\mathbf{K}_0, \mathbf{K}_G, z)$, where i labels the essentially different contributing paths–i.e. those for which $\mathbf{R}_0{}^i$ lies in the same unit cell (this does not imply that the *exit points* $\mathbf{R}_G{}^i(\mathbf{K}_0, \mathbf{K}_G, z)$ must lie within a single unit cell). The density ρ_i associated with the ith path is measured by the angular dispersion about $\mathbf{K}_G$ of the exit wave vectors of paths which enter with $\mathbf{K}_0$ at points near to $\mathbf{R}_0{}^i$, so that we may write

$$\rho_i = \left| \frac{\partial \mathbf{K}(\mathbf{R}_0, \mathbf{K}_0, z)}{\partial \mathbf{R}_0} \right|^{-1}_{(\mathbf{R}_0 = \mathbf{R}_0{}^i(\mathbf{K}_0, \mathbf{K}_G, z))}$$

$$= \left| \frac{\partial \mathbf{R}_0{}^i(\mathbf{K}_0, \mathbf{K}_G, z)}{\partial \mathbf{K}_G} \right|, \qquad (2.1)$$

where the derivatives denote the functional determinants (Jacobians) between K_x, K_y and R_{0x}, R_{0y}. If the phase along the ith path is $W_i(\mathbf{K}_0, \mathbf{K}_G, z)$, the interfering-classical-paths model predicts, for the required diffraction amplitudes

$$A_G(z, \mathbf{K}_0) = C \sum_i [\rho_i(\mathbf{K}_0, \mathbf{K}_G, z)]^{1/2} \times \exp\{iW_i(\mathbf{K}_0, \mathbf{K}_G, z)\}, \qquad (2.2)$$

where C is a normalization constant.

To find W_i and ρ_i we require the classical paths. Overall mass-energy conservation, together with neglect of $(\bar{U}(\mathbf{R})/k)^2$–this quantity rarely exceeds 10^{-2}–leads to the following expression:

$$\frac{\hbar^2}{2m}(K^2 + k_z{}^2 + \bar{U}(\mathbf{R})) = \text{const} = \frac{\hbar^2 k^2}{2m}. \qquad (2.3)$$

This has the form of a non-relativistic "Hamiltonian" with canonical coordinates **R**, z and momenta $\hbar\mathbf{K}$, $\hbar k_z$, but it must be remembered that $k(=2\pi/\lambda)$, $\bar{U}(\mathbf{R})$ and m are given by relativistic formulae (1.2), (1.4) and (1.5). Because z does not appear explicitly in (2.3), k_z is constant along each ray inside the crystal (although it varies from ray to ray) and Hamilton's equations for the time derivatives $\dot{z}$ and k_z give

$$z = \frac{\hbar k_z t}{m}, \quad k_z = (k^2 - K_0^2 - \bar{U}(\mathbf{R}))^{1/2}, \tag{2.4}$$

where the second equation comes from the initial condition at z = 0. Now we have already used the fact that $(\bar{U}(\mathbf{R})/k)^2$ is negligible, and the small-angle nature of all the processes here considered means that $(K_0/k)^2$ is very small also; thus k_z can be replaced by k in (2.4) and we have

$$z \approx \hbar k t/m, \tag{2.5}$$

so that z can be employed instead of the time t as a universal parameter characterising the rays. Expressing Hamilton's equations for $\dot{\mathbf{R}}$, $\hbar\dot{\mathbf{K}}$ in terms of z, we get

$$\left.\begin{aligned} &\frac{d\mathbf{R}(z)}{dz} = \frac{\mathbf{K}(z)}{k}; \\ &\frac{d\mathbf{K}(z)}{dz} = -\frac{\nabla_{\mathbf{R}}\bar{U}(\mathbf{R}(z))}{2k}; \\ &\mathbf{R}(0) = \mathbf{R}_0; \\ &\mathbf{K}(0) = \mathbf{K}_0, \end{aligned}\right\} \tag{2.6}$$

as the equations and boundary condition for the rays. It will be convenient to write (2.3) as

$$\begin{aligned} K^2 + \bar{U}(\mathbf{R}) &= \text{const along a ray} \equiv S \\ &= K_0^2 + \bar{U}(\mathbf{R}_0), \end{aligned} \tag{2.7}$$

where we have introduced the two-dimensional "energy" S for each ray.

To find the phase W_i from (2.6), it is necessary to use (1.1) to select the rays contributing to the Gth beam, and standard theory[7] gives

$$\begin{aligned} W_i(\mathbf{K}_0, \mathbf{K}_G, z) = &\frac{1}{\hbar}\int_0^{t(z)} dt\, \frac{\hbar^2}{2m}(K^2 - \bar{U}(\mathbf{R})) \\ &+ \mathbf{K}_0 \cdot \mathbf{R}_0{}^i - \mathbf{K}_G \cdot \mathbf{R}_G{}^i, \end{aligned} \tag{2.8}$$

where the first term is the usual one, involving the "Langrangian", and the other two terms arise because W_i refers to a family of rays defined by momenta rather than coordinates. By eliminating t using (2.5), introducing S from (2.7), and using (2.6), we obtained the more useful alternative forms

$$\begin{aligned} W_i(\mathbf{K}_0, \mathbf{K}_G, z) = &\frac{1}{2k}\int_0^z dz(K^2 - \bar{U}(\mathbf{R}(z))) \\ &+ \mathbf{K}_0 \cdot \mathbf{R}_0{}^i - \mathbf{K}_G \cdot \mathbf{R}_G{}^i \end{aligned} \tag{2.9}$$

$$\begin{aligned} &= \int_{\mathbf{R}_0^i}^{\mathbf{R}_G^i} \mathbf{K}(\mathbf{R}) \cdot d\mathbf{R} - \frac{zS^i}{2k} \\ &+ \mathbf{K}_0 \cdot \mathbf{R}_0{}^i - \mathbf{K}_G \cdot \mathbf{R}_G{}^i, \end{aligned} \tag{2.10}$$

where $\mathbf{R}_0{}^i$, $\mathbf{R}_G{}^i$ and S^i are all functions of $\mathbf{K}_0$, $\mathbf{K}_G$ and z. In Section 5 of I these classical formulae for W_i appeared as the end result of an asymptotic solution of Schrödinger's equation. An expression for the density ρ_i in terms of W_i can be found using the result[7]

$$\nabla_{\mathbf{K}_0} W_i(\mathbf{K}_0, \mathbf{K}_G, z) = \mathbf{R}_0{}^i(\mathbf{K}_0, \mathbf{K}_G, z), \tag{2.11}$$

so that (2.1) becomes

$$\rho_i(\mathbf{K}_0, \mathbf{K}_G, z) = \left|\det_{K_x K_y}\left\| \frac{\partial^2 W_i(\mathbf{K}_0, \mathbf{K}_G, z)}{\partial \mathbf{K}_0 \partial \mathbf{K}_G}\right\|\right|. \tag{2.12}$$

Micrographs showing $|A_G(z, \mathbf{K}_0)|^2$ as a function of z and $\mathbf{K}_0$ are characterized by vivid patterns of lines and spots. We believe that many features of these patterns can be explained by examining two basic properties of ρ_i and W_i, without working out all the details of the rays involved in (2.2). The first property concerns ρ_i: as we explore a micrograph–i.e. as we vary $\mathbf{K}_0$ and/or z, keeping **G** fixed, ρ_i will vary, and it is clear that any regions where ρ_i is infinite will dominate the observed intensity pattern. What is the nature of such regions? From (2.1), they occur whenever $|\partial\mathbf{K}/\partial\mathbf{R}_0|$ vanishes, i.e. when all the rays incident on a small area $d\mathbf{R}_0$ of the crystal emerge with the *same* direction $\mathbf{K}_G$. This behaviour is *focusing in momentum space*, and the regions in $(\mathbf{K}_0, z)$ space where it occurs are *envelopes of the paths*, i.e. loci of places where neighbouring contributing rays touch with a common tangent. On micrographs showing a two-dimensional section of $\mathbf{K}_0$, z space (e.g. the wedge and dome specimens shown in Figures 3 and 4) these singularities of ρ will be lines or points; we call them *caustics* (see Section 7.3 of II).

The singularities at caustics may of course be of different strengths. In particular, caustics of zero strength may occur–i.e. a set of paths may have an "envelope" where the path density is not infinite.

Figure 6 shows a real space example of this: an ensemble of balls under the action of gravity, all projected with the same initial velocity, bounces elastically off a horizontal surface. At the upper envelope ρ is infinite, while ρ is finite at the lower "envelope". This effect arises whenever reflection

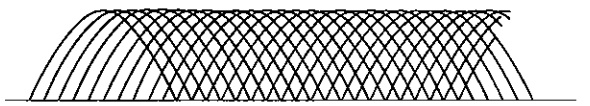

FIGURE 6 The two envelopes of paths of bouncing balls. The ground is a "caustic of zero strength."

occurs at a discontinuity, and we shall see in Section 3 that when there is a cusp in the one-dimensional potential $\bar{U}(x)$ (Figure 2), or when the curvature of $\bar{U}(x)$ at its minimum is large, the associated caustics are what we shall call "weak", and do not show up as bright lines on micrographs.

In general, however, caustics will dominate the micrographs. Indeed if the effects of the phases W_i can be ignored, they will be the only significant features, and

$$|A_{\mathbf{G}}(z, \mathbf{K}_0)|^2 = C^2 \sum_i \rho_i(\mathbf{K}_0, \mathbf{K}_{\mathbf{G}}, z), \qquad (2.13)$$

an expression which results from squaring (2.2) if the cross terms wash out by phase averaging. This corresponds to assuming pure classical mechanics with no interference effects. The importance of caustics is not sufficiently appreciated in classical mechanics, but let us quote from a recent text[8] on geometrical optics: "The caustic is one of the few things in geometrical optics that has any physical reality. Wavefronts and rays are not realizable; they are just convenient symbols on which we can hang our ideas. The caustic on the other hand is real and becomes visible by blowing a cloud of smoke in the region of the focus of a lens."

When interference is taken into account, however, wavefronts (but not rays) are "realizable", and this constitutes the second property of Eq. (2.2) giving rise to pattern on micrographs. In regions of $(\mathbf{K}_0, z)$ space free from caustics, if there are two or more contributing paths with comparable values of ρ_i, *interference fringes* will dominate the pattern; these are loci of constant difference between the corresponding phases W_i.

In the one-dimensional case of propagation among atomic planes, this scheme which predicts that the principal pattern features of micrographs are caustics and interference fringes can be fairly fully worked out analytically. The results appear in Section 3. In the two-dimensional case of propagation in a lattice of strings of atoms, the caustic structure of the classical paths which we discuss in Section 4, is very complicated; this suggests that interference phenomena will not be very important, and it is, in any case, certainly plausible that in more complicated cases the multitude of small perturbations acting on the electrons will tend to spoil the phase coherence, so that interference may be neglected.

In the analysis of heavy-particle channelling[4] there is, of course, no discussion of interference. But there is no discussion of caustics either; this is surprising at first but we must remember that the specimens used are often thicker, and the particle velocities slower, than in electron microscopy, so that the pattern of paths is much more complicated. Therefore there are many more caustics, and, given the lower resolution in channelling experiments, it becomes justified to use an "ergodic theorem" which states that the paths have explored all accessible regions of phase space so that caustics are "everywhere dense". Thus classical statistical mechanics is employed, rather than the more deterministic analysis required by electron microscopy. In the future, as electron microscopy explores thicker specimens, and particle channelling becomes more precise, an analysis of the transition regime may be needed (see also Section 4).

3 INTERFERING CLASSICAL PATHS–PROPAGATION IN A LATTICE OF ATOMIC PLANES

In this case the potential $\bar{U}(x)$ is one-dimensional, and takes the form shown in Figure 2. The character of the classical paths depends fundamentally on whether the two-dimensional "total energy" S, introduced in Eq. (2.7), is positive or negative. To see this, we write, for the direction $K(x)$,

$$K^2(x) = S - \bar{U}(x). \qquad (3.1)$$

Now $\bar{U}(x)$ is never positive; it ranges from zero to $-|\bar{U}(a/2)|$ (see Figure 2). Therefore if S is *positive* $K^2(x)$ is positive for all x, and $K(x)$ can never change sign–i.e. the particle never reverses the direction of its motion along ox. As z increases, therefore, the electron moves from cell to cell in the one-dimensional lattice (Figure 7). We say that electrons with $S > 0$ move along *nearly-free paths*. When S is *negative*, however, then, provided $S > -|\bar{U}(a/2)|$, there are regions of the potential barrier for which $K^2(x)$ is negative (Figure 7). These are classically inaccessible to an electron, which must, therefore, always remain confined to the potential well in which it started. We say that electrons for

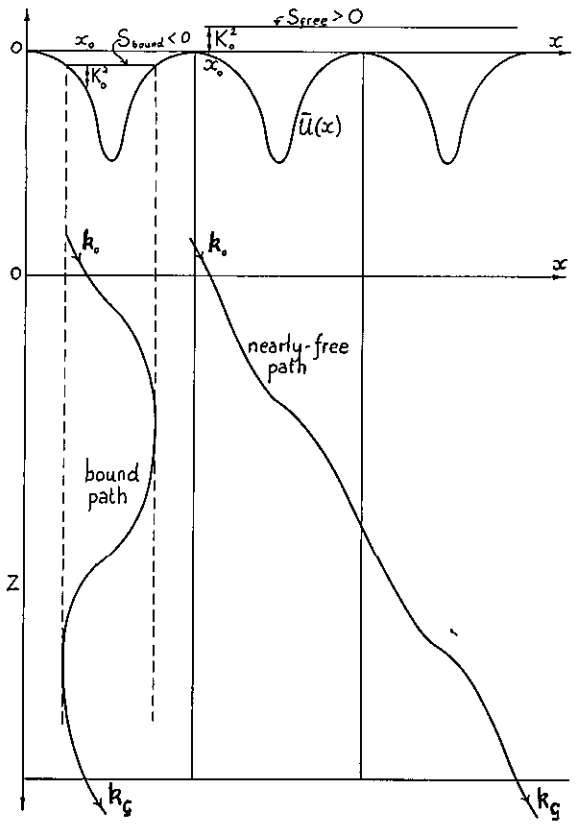

FIGURE 7 The two fundamental types of classical path among planes.

which $S < 0$ move along *bound paths*. If $S < -|\bar{U}(a/2)|$, no classical paths are possible.

The characteristic features of bound paths are *turning points*; these are values of x for which $S = \bar{U}(x)$, so that, from (3.1), $K(x)$ is zero. It is at turning points that $K(x)$ changes sign, enabling the electron to remain confined within one cell. Nearly free paths possess no turning points. Thus only bound paths can give rise to "reflected diffracted beams", for which K_G/K_0 is negative.

To find the types of path contributing at any particular orientation K_0, we use the fact (Eq. (2.7)) that the "energy" S for a path is given by $K_0^2 + \bar{U}(x_o)$. There are electrons incident on the crystal for all x_o, so that $\bar{U}(x_o)$ can take any value from $-|\bar{U}(a/2)|$ to zero. Thus, for a given K_0, the "energies" of the paths satisfy

$$K_0^2 - |\bar{U}(a/2)| \leqslant S \leqslant K_0^2. \tag{3.2}$$

If K_0 is zero (normal incidence on the crystal), S is always negative, and all paths are bound. If K_0^2 exceeds a critical value K_c^2, where

$$K_c^2 \equiv |\bar{U}(a/2)|, \tag{3.3}$$

then S is always positive, and all paths are nearly-free. If $0 < K_0^2 < K_c^2$ some paths are bound and some are nearly-free. In electron microscopy K_c is generally a few times greater than the reciprocal lattice spacing $2\pi/a$ (i.e. the "critical angle" $\theta_c = K_c/k$ is generally several times the Bragg angle), and in most micrographs the range of K_0 displayed generally does not extend out as far as $\pm K_c$. The "critical angle" of heavy-particle channelling theory[4] is simply K_c/k–typically a few degrees for electrons.

Now let us investigate which diffracted beams G may appear when the direction of incidence is K_0. The direction of emergence K_G is $K_0 + G$, and G is $2\pi n/a$, where n is an integer (positive or negative). Let the possible G-values range from $G_{min}(<0)$ to $G_{max}(>0)$. Then if K_0 is chosen positive (this involves no loss of generality) Eqs (3.1) and (2.7) imply that

$$\begin{aligned} G_{max} &= (K_0^2 + \bar{U}(x_0) - \bar{U}(x_G))_{max}^{1/2} - K_0 \\ &= (K_0^2 + K_c^2)^{1/2} - K_0, \end{aligned} \tag{3.4}$$

for both bound and nearly-free paths. The "most positively-deviated path" is incident on an interatomic potential barrier (e.g. $x = 0$), and emerges at an atomic plane (e.g. $x = a/2$). For G_{min} the situation is different for $K_0 \gtrless K_c$. If $K_0 > |K_c|$ all paths are nearly-free, so that K_G must be positive, and

$$\begin{aligned} G_{min} &= (K_0^2 + \bar{U}(x_0) - \bar{U}(x_G))_{min}^{1/2} - K_0 \\ &= -(K_0 - (K_0^2 - K_c^2)^{1/2}) \quad (K_0 > |K_c|) \end{aligned} \tag{3.5}$$

The "most negatively-deviated path" is incident on an atomic plane, and emerges at an interatomic barrier. If $K_0 < |K_c|$ the "most negatively-deviated path" is a bound path with negative K_G, so that

$$\begin{aligned} G_{min} &= -|K_G|_{max} - K_0 \\ &= -(K_0 + |K_c|) \quad (K_0 < |K_c|) \end{aligned} \tag{3.6}$$

where we have used the fact (3.1) that the appropriate path has $S = 0$ and emerges at an atomic plane.

The results (3.4–3.6) are summarized in Figure 8, which enables the extent of the "fan" of diffracted beams to be read off immediately for any K_0. Alternatively, for any diffracted beam G, Figure 8 shows the range of orientations K_0 over which "bend contours" can be expected on the corresponding diffraction contrast micrograph, taken in the manner described in Section 1; the limiting K_0-values are symmetrical about $-G/2$, and it can be shown that this result is expected

from the reciprocity theorem which holds for particles or waves. The predictions of Figure 8, in particular the effects of the critical direction K_c, have been confirmed by experiment.[9]

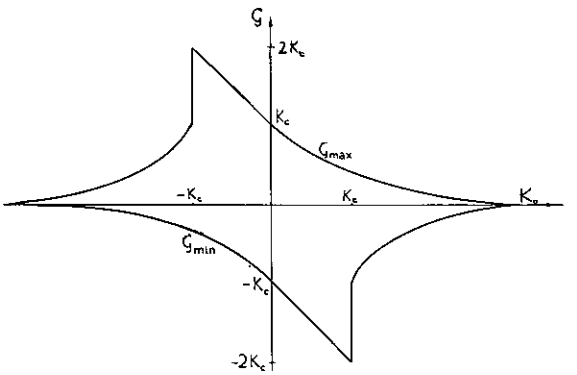

FIGURE 8 Construction for limiting diffracted beams G_{min} and G_{max} for each orientation K_0.

To understand bend contours in detail, rather than simply the range of directions K_0 within which they appear on micrographs, it is necessary to make a finer classification of the paths within the broad scheme of "bound" and "nearly-free". The paths which suffer a deflection G must be divided into families, each family contributing to a region of the z, K_0 plane. The boundaries of these regions are the caustics of the family, and can be expected to appear as bright lines on the diffraction contrast micrograph for the Gth beam unless the caustics are "weak" in the sense described in Section 2 (cf. Figure 6).

To find the families, and their contributing regions, it is necessary to solve the equations (2.6) for the paths; in terms of S (Eq. (2.7), we have, in one dimension.

$$\frac{z}{k} = \int_{x_0{}^i}^{x_G{}^i} \frac{\mathbf{dx}\cdot\hat{\mathbf{K}}}{|\mathbf{K}|} = \int_{x_0{}^i}^{x_G{}^i} \frac{\mathbf{dx}\cdot\hat{\mathbf{K}}}{(S-\bar{U}(x))^{1/2}}, \tag{3.7}$$

where $\hat{\mathbf{K}}$ is the unit vector along $\mathbf{K}$. The vector notation has been used to emphasize the fact that a *path integral* is involved—for a bound path $x_0{}^i$ and $x_G{}^i$ may be the same, but the integral is not zero because the particle may emerge after reflection at a turning point. If S, K_0 and K_G are fixed, x_0 and x_G are restricted by (3.1) and the periodicity and symmetry of $\bar{U}(x)$ Figure 2) to take the values

$$\left.\begin{aligned} x_0 &= \pm x_0{}^+ + m_1 a \\ x_G &= \pm x_G{}^+ + m_2 a \end{aligned}\right\}, \tag{3.8}$$

where $x_0{}^+$ and $x_G{}^+$ lie between 0 and $a/2$, and m_1 and m_2 are integers. Without loss of generality we can take $m_1 = 0$ and K_0 positive. The path equation (3.7) can now be written explicitly for *nearly-free paths* as

$$\frac{z}{k} = 2m\int_0^{a/2} \frac{dx}{(S-\bar{U}(x))^{1/2}} \pm \int_0^{x_0{}^+} \frac{dx}{(S-\bar{U}(x))^{1/2}} \pm \int_0^{xG^+} \frac{dx}{(S-\bar{U}(x))^{1/2}}, \tag{3.9}$$

where m is any non-negative integer (which measures the number of times the path crosses an atomic plane) and the two ± signs are independent. For *bound paths* the same equation holds, with the lower limits of the integrals replaced by the turning point $x_t{}^+$, this being the solution of $S = \bar{U}(x)$ lying between 0 and $a/2$; now the ± signs are not independent—for even m we must have +− or −+ if $K_0/K_G > 0$ and −− or ++ if $K_0/K_G < 0$. Thus for each non-zero value of m there are six families of paths, two bound and four nearly-free.

We do not intend here to discuss all the families of paths specified by m, ±, ±, or the special case of paths with $m = 0$; the algebra is heavy and the details will be published elsewhere. Instead we shall confine ourselves to the "bright-field" case $G = 0$ (that is, we consider paths which have suffered no net deflection and contribute to the beam which has suffered no net diffraction). Further, we only consider one family each of bound and nearly-free paths.

In (3.9) consider the family of nearly-free paths with $(m, -, +)$; a typical path of this family is sketched in Figure 9. Since $G = 0$, $x_0{}^+$ and $x_G{}^+$ are the same, and the equation is simply

$$\frac{z}{k} = 2m\int_0^{a/2} \frac{dx}{[S-\bar{U}(x)]^{1/2}}. \tag{3.10}$$

The region of the z, K_0 plane within which this family exists can be found by letting S sweep through its permitted values, given by (3.2). For a given value of K_0 the smallest z for which the path exists corresponds to the largest value of S, namely $K_0{}^2$, which occurs when $x_0{}^+$ is zero—i.e. the electrons enter and leave on an interatomic barrier. The largest z corresponds to the smallest S, namely $K_0{}^2 - K_c{}^2$ if $K_0 > K_c$, or zero if $K_0 < K_c$, which occurs when $x_0{}^+$ is $a/2$—i.e. the electrons enter and leave on an atomic plane. Thus the

"envelopes" of the family are

$$\left.\begin{aligned} \frac{z_{min}(K_0)}{k} &= 2m\int_0^{a/2}\frac{dx}{(K_0^2-\bar{U}(x))^{1/2}} \quad \text{(a)} \\ \frac{z_{max}(K_0)}{k} &= 2m\int_0^{a/2}\frac{dx}{(K_0^2-K_c^2-\bar{U}(x))^{1/2}} \\ &\qquad (|K_0|>|K_c|) \quad \text{(b)} \\ &= \infty \qquad (|K_0|<|K_c|) \end{aligned}\right\}. \tag{3.11}$$

These curves are sketched in Figure 10.

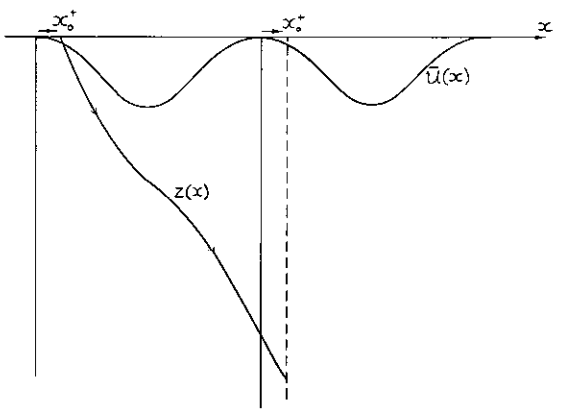

FIGURE 9 Sketch of the nearly-free path 1, –, +.

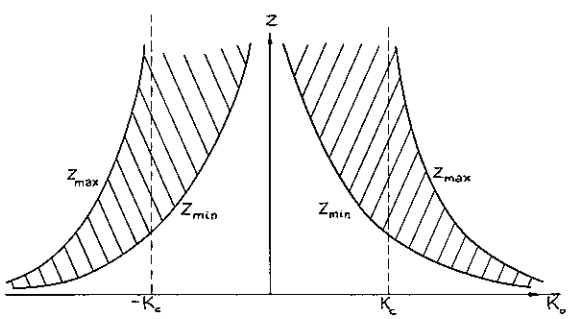

FIGURE 10 Region (shaded) in which the nearly-free path $(m, -, +)$ exists for $G = 0$.

The line $z_{min}(K_0)$ at which the path appears as z increases is a caustic, at which the path density ρ can easily be shown to be infinite. Thus we expect to find "bend contours" for each value of m–i.e. a series of bright lines whose separation in z at fixed K_0 is

$$\Delta z(K_0) = 2k\int_0^{a/2}\frac{dx}{(K_0^2-\bar{U}(x))^{1/2}}. \tag{3.12}$$

The line $z_{max}(K_0)$, on the other hand, is associated with the atomic planes, where $\bar{U}(x)$ has cusps (Figure 2) or sharp minima (Figure 7), and it can be shown that these correspond to "weak caustics", where ρ is either finite or else diverges weakly. Thus we do not expect $z_{max}(K_0)$ to appear as lines on the micrograph –particularly since in any region where a search might be made for z_{max} there will always be a z_{min} (corresponding to a larger value of m) which will dominate.

The other types of nearly-free path are not so easy to analyse, but the results are similar, and we again predict series of strong caustics given either by Eq. (3.11a) or by a closely similar equation.

What about bound paths? For our typical family we take (even m, –, +), of which an example is sketched in Figure 11. From (3.9) we get, as the path equation

$$\frac{z}{k} = 2m\int_{x_t^+(s)}^{a/2}\frac{dx}{(S-\bar{U}(x))^{1/2}}, \tag{3.13}$$

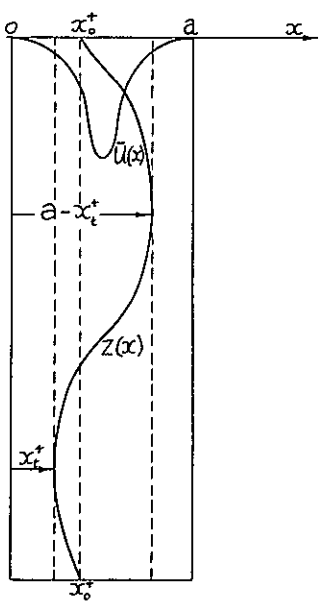

FIGURE 11 Sketch of bound path 2, –, +.

where $x_t^+(S)$ is the turning point. S is now negative, and for a given K_0 its value sweeps from $K_0^2 - K_c^2$ to zero as x_0 varies. The maximum value of z is infinite, corresponding to $S = 0$. The expression for $z_{min}(K_0)$ depends on the form of $\bar{U}(x)$; if the potential is cusp-

shaped as in Figure 2, with a curvature everywhere negative, then

$$\frac{z_{\min}(K_0)}{k} = 2m \int_{x t^{+}(K_0^2 - Kc^2)}^{a/2} \frac{dx}{(K_0^2 - K_c^2 - \bar{U}(x))^{1/2}}, \tag{3.14}$$

a curve sketched in Figure 12. The line z_m is the envelope of the family being considered, but it is not a caustic, since the particles involved enter and leave the crystal on an atomic plane, and ρ can be shown to be finite. If the cusps are smoothed out into sharp minima, $z_{\min}(K_0)$ does not quite reach down to zero at $K_0 = 0$ but its form resembles that shown in Figure 12, and the envelope is a weak caustic, which may be ignored. Similar results hold for the other families of bound paths.

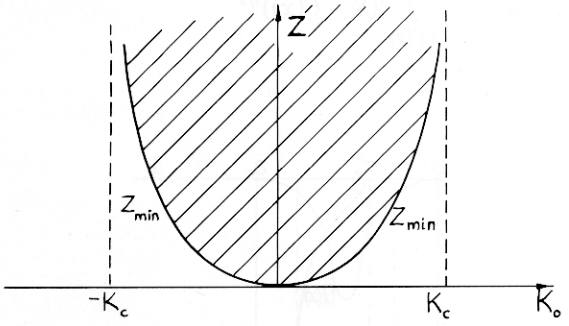

FIGURE 12 Region (shaded) in which the bound path (even m, –, +) exists for $G = 0$.

Since the bound paths never show strong caustics, it follows from the arguments of Section 2 that their contributions will be dominated by *interference fringes*, which will, however, only be prominent in regions where there are no caustics from the nearly-free paths. There is only one such region, and that is the unshaded area below $z_{\min}(K_0)$ for $m = 1$ on Figure 10. The interference fringes will be "almost periodic functions" resulting from the superposition of a large number of contributions of the form (2.2) (for a "cusp" potential an infinite number of bound paths contribute for $K_0 = 0$, since (3.9) then has solutions for all m, whatever the value of z–see Section 5 of I).

We are now in a position to test the "interfering classical path" model against experiment. Figure 13 shows (schematically) the predicted bend contours–caustics of the nearly-free paths away from $K_0 = 0$, and fringes from the bound paths near $K_0 = 0$. Figure 14 shows an experimental bright-field micrograph–Gold

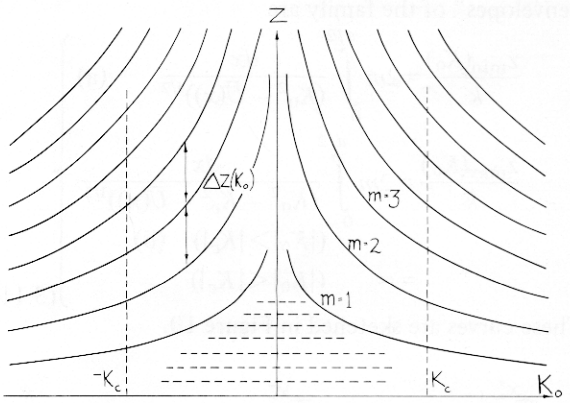

FIGURE 13 Schematic predicted bend contours for $G = 0$. ———— caustics - - - - - - - - - interference fringes.

at 600 kV, reflections from 111 planes. The contours are typical of micrographs taken under "many-beam" conditions–i.e. those which from our point of view

FIGURE 14 Bright-field micrograph, gold (111) 600 kV ($K_c = 2\pi/a \times 2.93$). Courtesy of Dr. C. J. Richards.

are the most likely candidates for a semiclassical treatment. It is obvious that the theory we have been elaborating does indeed predict correctly the principal features shown by micrographs.

The similarity of Figures 13 and 14 is reinforced by a quantitative comparison. Table I compares the *caustic*

spacing $z(K_0)$ predicted by Eq. (3.12) with the mean of those observed, for three different values of K_0; the degree of agreement is somewhat startling. For the *interference fringes*, the observed spacing at $K_0 = 0$ (normal incidence) is 175 Å, while the theoretical spacing, obtained by measurement from a curve of superposed path contributions of the form (2.2), is 181 Å.

TABLE I

Direction K_0/K_c	Mean observed line spacing Å	Theoretical caustic spacing $\Delta z(K_0)$ (Å)
0.178	506	431
0.307	331	339
0.477	243	254

These preliminary calculations do suggest that the "interfering classical path" description is a valid, albeit unfamiliar, alternative to the exact "interfering Bloch wave" series, which will be discussed in Sections 5, 6 and 7. Perhaps the most unexpected feature of the model is the regular sequence of caustics which originates in the periodicity of $\bar{U}(x)$, and which does not occur in any other application of classical mechanics, so far as we know. The simple form of Eq. (3.11a), which gives the form of the caustics, suggests that some sort of inversion procedure might be possible, to enable the potential $\bar{U}(x)$ to be reconstructed. A formal inversion is possible, but it involves complex values of K_0, indicating that (3.11a) is, mathematically, an "ill-conditioned" equation–i.e. the caustics are relatively insensitive to $\bar{U}(x)$ for real x, and the method is impractical.

Not all the features of micrographs are predicted by the considerations advanced in this section; for example inspection of Figure 14 shows that some of the "caustics" coalesce at certain points. It may be that such details can be explained on the interfering path model, if interference effects are not neglected near caustics. To test this, work is in progress to calculate full simulations of the bright-field micrographs, using Eq. (2.2) directly, and also including extra phase factors of multiples of $\pi/2$ which this expository account has ignored, but which arise in practice whenever rays pass through spatial caustics in the course of their propagation (see Section 5 of I and Section 7.3 of II).

4 INTERFERING CLASSICAL PATHS-PROPAGATION IN A LATTICE OF ATOMIC STRINGS

When the specimen is dome-shaped as in Figure 4, the diffraction contrast images show a far more intricate fine structure than those from bent wedge specimens (Figures 3, 14). Figure 15 shows a typical example of

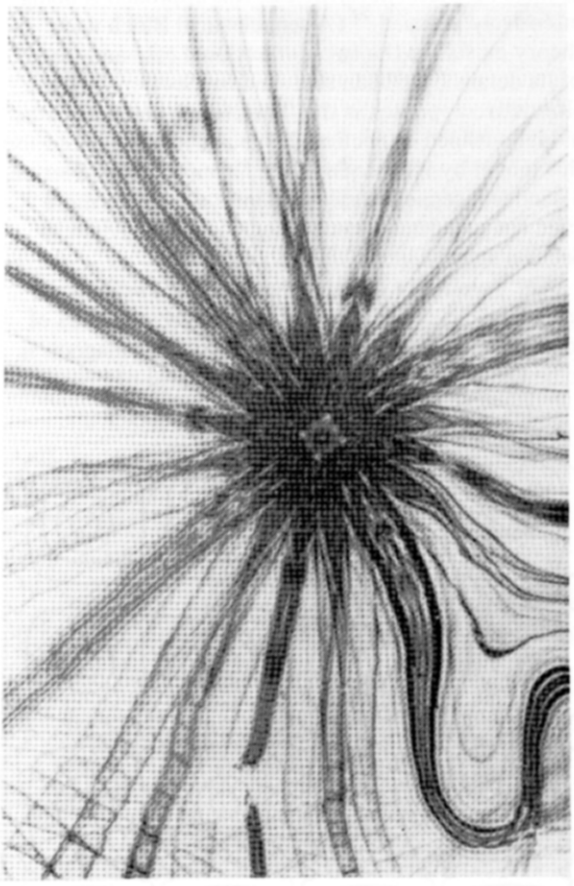

FIGURE 15 Bright-field micrograph of the (100) pole of tungsten at 750 kV. Courtesy of Dr. M. S. Spring.

this, taken in the "bright field" $\mathbf{G} = 0$ (Eq. (1.1) ff). The pattern has fourfold symmetry about a centre (the "pole"). What we wish to explain is the detail near the pole, which is due to electrons incident almost parallel to the (100) strings of atoms ($\mathbf{K}_0 \approx 0$). This detail is very sensitive to the shape and strength of the potential $\bar{U}(\mathbf{R})$, and so constitutes a potentially powerful source of information about the crystal. (The "arms" radiating out from the pole are due to electrons incident almost parallel to *planes* of atoms, and the fine structure of oscillations of intensity across these arms arises in the

manner discussed in Section 3–from the caustics encountered on Figure 13 as K_0 is varied on Figure 13, z being kept constant.)

The theory required to interpret detail like that near the pole of Figure 15 is still in its infancy so that this section will be largely speculative. Conventional wave theory, while exact, requires the diagonalization of huge matrices; nevertheless, this approach is being intensively pursued.[25] (A semiclassical Bloch wave theory exists for the two-dimensional case and many of its details have been sketched in (Section 5).) The alternative approach is the "interfering classical paths" model outlined in Section 2. We are encouraged to use this model by its success in the "planar" case (Section 3); indeed, semiclassical mechanics should be more valid for two-dimensional cases, as we shall learn in Section 5 (see Eq. (5.17) ff).

The potential $\bar{U}(\mathbf{R})$ represents a two-dimensional array of wells centred on atomic strings; contours of constant $\bar{U}$ are sketched in Figure 16. This diagram is to be thought of as covered with a swarm of "particles"

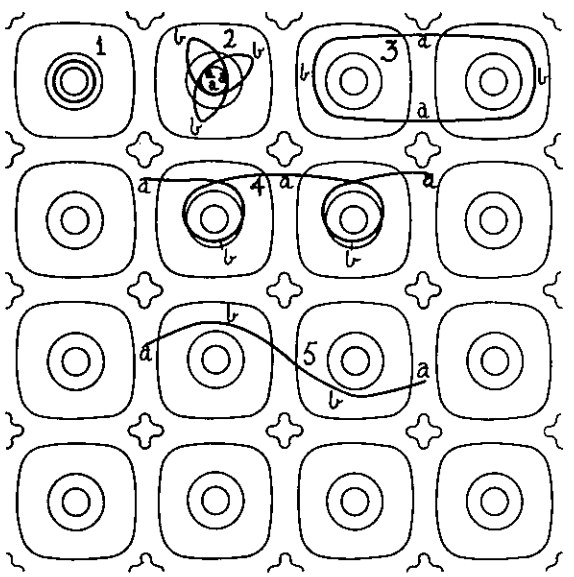

FIGURE 16 Contours of constant $U(\mathbf{R})$ (thin lines) for a "cross grating" case, with some typical contributing classical paths (thick lines) giving caustics on the bright-field micrograph

which started out at z = 0 uniformly distributed in the plane, but all with the same "momentum" $\mathbf{K}_0$. The particles move along classical paths $\mathbf{R}(z)$ according to Eqs (2.6). In the "final state", when z equals the crystal thickness, the positions R and "momenta" K are "frozen". The distribution of K-vectors is then related to what would be observed in a heavy-particle "star" channelling pattern (see, however, the remarks about inelastic effects in Section 1). For a diffraction contrast micrograph formed with the Gth beam as explained in Section I only those paths for which $\mathbf{K} = \mathbf{K}_G$ (Eq. (1.1)) will contribute. We shall restrict ourselves to the "bright-field" case, so we are only interested in those "particles" of the swarm for which the initial and final momenta equal $\mathbf{K}_0$, and the micrograph image intensity $|A_0(z, \mathbf{K}_0)|^2$ is given by Eq. (2.13) involving the "path density" $\rho_t(\mathbf{K}_0, \mathbf{K}_0, z)$ given by (2.1), or by Eq. (2.2).

Obviously the classical paths among strings will be much more complicated than among planes, and we shall see that the *caustics*, which dominate the micrographs as explained in Section 2, are much more densely distributed over the image plane K_{ox}, K_{oy} of the two-dimensional case than over the plane K_0, z (Figure 13) of the one-dimensional case. This suggests that some kind of "ergodic" situation may have been reached, where the approximation often employed in heavy-particle channelling[4] is valid; this states that on each "energy shell", specified by a value of S defined by Eq. (2.7), the electrons are uniformly distributed in the four-dimensional phase space R, K. The distribution among the different energy shells is determined by the phase-space density $\delta(\mathbf{K} - \mathbf{K}_0)$ which corresponds to the incident beam. Unfortunately, this approach is unlikely to succeed in the present problem, for at least three reasons: (i) we are dealing with thin crystals, so that even though the paths may be complicated, it is unlikely that the ergodic state has been reached. As an example, at the maximum orientation $|\mathbf{K}_0|$ on Figure 15 at which the electrons see strings rather than planes (about halfway out to where the "arms" appear) the electrons can have traversed only a few "unit cells" in the R plane in their journey through the crystal ($z \sim 700$ Å). (ii) Even for thick specimens it is by no means certain that ergodicity is ever attained for initial phase-space distributions as sharply localized as $\delta(\mathbf{K} - \mathbf{K}_0)$. Recent research[26] suggests that there may be some non-separable systems for which particles always remain confined to a sub-domain of the "energy shell"–perhaps this indicates the existence of hitherto unsuspected "constants of the motion" apart from S. (iii) The "energy shells" in phase space are not all simply-connected: some consist of disconnected "sheets" (in the "planar" case *all* "energy shells" in the phase space x, K_0 are of this character). Even if ergodicity is assumed, it can only apply on each sheet separately. Thus if in the initial distribution $\delta(\mathbf{K} - \mathbf{K}_0)$ there are "particles" on one of the sheets

belonging to a given S, but none on another sheet belonging to the same S, then in the ergodic state the first sheet is uniformly covered by phase points, but the second is still empty. It appears to be very difficult to allow for this "topological" aspect of the situation in the two-dimensional case, and nonsensical results are obtained if it is ignored.

We conclude that there is no alternative to examining the classical paths in detail, selecting that set which contributes to the micrograph, and, in particular, the subset of paths giving rise to caustics (Section 2). The contributing paths R(z) start out with direction $\mathbf{K}_0$ and end with direction $\mathbf{K}(z) = \mathbf{K}_0$, moving meanwhile through regions of varying potential $\bar{U}(\mathbf{R}(z))$. We can show that those contributing paths for which the potential along the path has an extremal value at the beginning and end of the path correspond to caustics, and their contributions should appear bright on the micrographs (there are other types of caustic which we shall not describe here).

On Figure 16 are sketched what we think should be the principal contributing paths giving caustics, and on Figure 17 are sketched the expected lines and

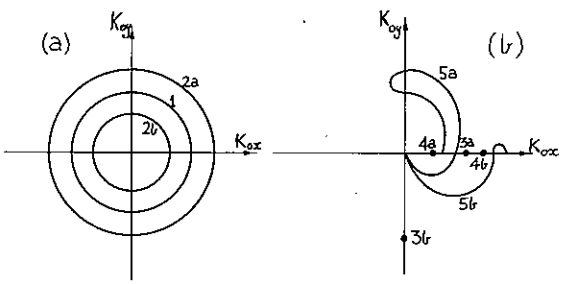

FIGURE 17 Caustics on micrograph for paths in Figure 16(a) paths with $S < 0$ (b) paths with $S > 0$.

spots which should result on the bright-field micrograph image plane K_{ox}, K_{oy}. These sketches are based on computed paths in a model potential $\bar{U}(\mathbf{R})$ made of "muffin tin" string potentials with cylindrical symmetry, cut off at some finite radius, with zero potential between the strings. Paths 1 and 2 have negative "energy" S, and so are bound within a single potential well. The beginning and end points must coincide (to make $\mathbf{K}(z) = \mathbf{K}_0$), and for path 2 must be either a or b (so that $\bar{U}(\mathbf{R})$ is an extremum). Bound orbits which are not closed (i.e. open "rosettes") cannot give caustics. The lines ab on path 2 may have any orientation and path 1 is symmetric so these paths give circles on the micrograph (Figure 17a). In the case of type 1 paths the circles should appear on the micrograph at values of $|\mathbf{K}_0|$ which satisfy

$$\frac{d\bar{U}}{d|\mathbf{R}|}\left(|\mathbf{R}| = \frac{z}{2\pi k}|\mathbf{K}_0|\right) = \frac{4\pi k}{z}n^2|\mathbf{K}_0|, \qquad (4.1)$$

n being any integer. Calculations with a string potential appropriate to Tungsten (100) at 750 kV give one solution of this equation ($n = 1$) and the resulting $|\mathbf{K}_0|$ corresponds to a circle about 1.5 times bigger than the diffuse ring just inside the four bright spots near the pole of Figure 15.

Paths 3, 4 and 5 have $S > 0$ and are not confined to a single cell; therefore these paths can display the symmetry of the lattice. Path 3 is closed, and "bound" to two adjacent strings. Again the end-points must coincide, and may be any of the points marked a or b on Fig. 16. On the micrograph, the path gives rise to spots shown on Figure 17b. Paths 4 and 5 are open, and the end-points may be any pair of points marked a, or any pair marked b, in Figure 16. In path 4, $\mathbf{K}_0$ lies along principal lattice directions, so that on the micrograph plane (Figure 17b) spots appear as marked. In path 5, $\mathbf{K}_0$ need not lie along lattice directions, and the peculiar line caustic shown in Figure 17b results from this. To allow for all paths of type 3, 4 and 5 permitted by the symmetry, Figure 17b should be reflected successively in both axes. Also, to allow for paths like 3, 4 and 5 which involve second-nearest-neighbour strings, there should be superimposed on Figure 17b a similar figure on a slightly different scale, rotated through 45° (for this "square" case). We ignore all paths involving 3 or more strings, because specimens are generally not thick enough for these to contribute near the pole of the micrograph (where $|\mathbf{K}_0|$ is small).

Combining Figures 17a and 17b (after suitable reflections and rotation) the resulting predicted micrograph contains the following caustic structure: diffuse rings, spots along principal lattice directions, and winding lines from type 5 paths. The rings have already been discussed (they are in fact much more prominent on some other micrographs we have seen). The spots are clearly evident on Figure 15, and some qualitative success has been obtained in fitting their positions using a reasonable string potential; more precise calculations are currently being carried out. However, nothing like the "type 5" lines has been observed. Perhaps they are not resolved, and so contribute to a diffuse background illumination. Alternatively, these lines might be "weak caustics" (cf Section 2); more precise criteria for accepting or rejecting caustics are currently being developed (for example, places where "type 5" caustics cross might appear as bright spots).

It therefore appears that we have the outlines of a testable scheme of interpretation for cross-grating micrographs. Two points should be emphasized: first, the method does not rely on paths passing very close to the atomic strings; in this case the elastic scattering model (and also the string potential itself[4]) breaks down and the electrons are likely to be "absorbed" by inelastic scattering (see Section 6). Second, the classical paths elaborated here are very different from (and much more complicated than) those for positively-charged particles such as protons (where there are, for example, no "bound" states of a single string).

5 TOWARDS THE WAVE THEORY– UNDERSTANDING THE BLOCH WAVES

The classical paths we have been describing play no role in the orthodox analysis of electron diffraction contrast microscopy, which is based squarely on wave theory. But semiclassical methods, in the form of asymptotic approximation techniques applied to Schrödinger's equation, greatly increase our understanding of quantities appearing in the wave theory, as well as explaining how the transition to the "interfering classical path" model of Sections 2–4 occurs.

Let the electron wave function in the crystal be $\psi(\mathbf{r})$, which satisfies a relativistic time-independent wave equation with fixed kinetic energy E (the voltage through which the electron beam has been accelerated). Then it is shown in Section 2 of I that if the predominant z dependence of $\psi(\mathbf{r})$ is removed by the substitution

$$\psi(\mathbf{r}) = e^{ikz}\tau(\mathbf{R}, z) \tag{5.1}$$

then $\tau(\mathbf{R}, z)$ satisfies the following approximate equation valid at high energies

$$\left.\begin{aligned}[-\nabla_{\mathbf{R}}^2 + \bar{U}(\mathbf{R})]\tau(\mathbf{R}, z) &= 2ik\frac{\partial\tau}{\partial z}(\mathbf{R}, z)\\ \tau(\mathbf{R}, 0) &= e^{i\mathbf{K}_0\cdot\mathbf{R}}\end{aligned}\right\}, \tag{5.2}$$

where the boundary condition comes from matching the incident and crystal waves. This has the form of a two-dimensional wave equation with "Hamiltonian" $-\nabla_{\mathbf{R}}^2 + \bar{U}(\mathbf{R})$ (cf. 2.7) with z acting as a "time" variable.

It is easy to eliminate the z dependence of (5.2) by expanding $\tau(\mathbf{R}, z)$ as an eigenfunction series:

$$\tau(\mathbf{R}, z) = \sum_j C_j\tau_j(\mathbf{R})\, e^{-iS_jz/2k}, \tag{5.3}$$

where C_j are constants for a given $\mathbf{K}_0$ and $\tau_j(\mathbf{R})\, e^{-iS_jz/2k}$ are the *Bloch waves*, which satisfy

$$(-\nabla_{\mathbf{R}}^2 + \bar{U}(\mathbf{R}))\tau_j(\mathbf{R}) = S_j\tau_j(\mathbf{R}). \tag{5.4}$$

The *eigenvalues* S_j are the quantized values of the "two-dimensional energy" S, introduced in Eq. (2.7), determined by the requirement that $\tau_j(\mathbf{R})$ is smooth and satisfies the Bloch condition

$$\tau_j(\mathbf{R} + \mathbf{R}_l) = e^{i\mathbf{K}_0\cdot\mathbf{R}_l}\tau_j(\mathbf{R}), \tag{5.5}$$

$\mathbf{R}_l$ being any lattice vector in the "projected crystal" defined by $\bar{U}(\mathbf{R})$. We also require $\tau_j(\mathbf{R})$ to be normalized over a unit cell of the lattice. Thus the S_j depend on $\mathbf{K}_0$, and if $S_j(\mathbf{K}_0)$ is plotted vertically above the horizontal plane defined by K_{ox}, K_{oy}, the result is the *dispersion surface*, on which the wave theory is based. (In the "systematic diffraction" case of propagation among planes, $S_j(\mathbf{K}_0)$ is simply a set of curves.) If we Fourier-analyze the wave function $\tau(\mathbf{R}, z)$ (Eq. (5.3)) at the exit face of the specimen, we obtain $A_{\mathbf{G}}(z, \mathbf{K}_0)$, the amplitude of the **G**th diffracted beam. After choosing C_j to satisfy the boundary condition in (5.2), we get

$$A_{\mathbf{G}}(z, \mathbf{K}_0) = \sum_j \left(\iint_{\substack{\text{unit}\\ \text{cell}}} d\mathbf{R}\tau_j^*(\mathbf{R})\, e^{i\mathbf{K}_0\cdot\mathbf{R}}\right) \times\left(\iint_{\text{unit}} d\mathbf{R}\tau_j(\mathbf{R})\, e^{-i\mathbf{K}\mathbf{G}\cdot\mathbf{R}}\right) e^{-iS_j(\mathbf{K}_0)z/2k}, \tag{5.6}$$

where $\mathbf{K}_{\mathbf{G}}$ is given by (1.1).

This expression for $A_{\mathbf{G}}(z, \mathbf{K}_0)$ as a series of eigenfunctions is the fundamental result of the wave theory. At the end of this section we shall describe how it can be transformed into the totally different series of interfering classical paths (Eq. (2.2)), but it is necessary to understand Eq. (5.6) first. The central problem is the determination of $S_j(\mathbf{K}_0)$. Conventionally,[3] the periodic potential $\bar{U}(\mathbf{R})$ is expanded in a Fourier series

$$\bar{U}(\mathbf{R}) = \sum_{\mathbf{G}} U_{\mathbf{G}}\, e^{i\mathbf{G}\cdot\mathbf{R}}, \tag{5.7}$$

and $\tau_j(\mathbf{R})$ is expanded also. Then Eqs. (5.4) and (5.5) give rise to the "secular equation" for $S_j(\mathbf{K}_0)$ namely

$$\det_{\mathbf{G}\mathbf{G}'}\|[S_j(\mathbf{K}_0) - (\mathbf{K}_0 + \mathbf{G})^2]\delta_{\mathbf{G}\mathbf{G}'} - U_{\mathbf{G}-\mathbf{G}'}\| = 0. \tag{5.8}$$

The electron energy E occurs in the relativistic mass factor multiplying $U_{\mathbf{G}-\mathbf{G}'}$ (Eqs. (1.4), (1.5)). As E increases, so does $|U_{\mathbf{G}-\mathbf{G}'}|$ and off-diagonal terms in

(5.8) become more important and eventually dominate. Thus computer calculations of the dispersion surface $S_j(\mathbf{K}_0)$ become more difficult as E increases. Furthermore, it becomes increasingly difficult to understand the form of $S_j(\mathbf{K}_0)$ in terms of the U_G's, as they emerge from the computer.

We look at the problem differently; instead of expanding $\bar{U}(\mathbf{R})$ as in Eq. (5.7), we examine the waves in *real space* as they scatter among the planes or strings of atoms. The one-dimensional case of planes is simplest, and we examine it first. Between two atomic planes lies a potential barrier $\bar{U}(x)$(Figure 18) of height K_c^2 where K_c is the classical "critical direction", defined by (3.3). A one-dimensional wave of unit amplitude

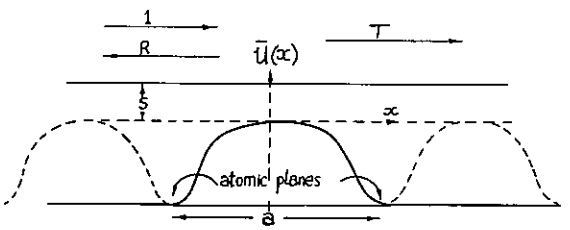

FIGURE 18 Reflection and transmission from an interatomic barrier.

incident on this barrier with "energy" S will be reflected with (complex) amplitude $R(S)$ and transmitted with (complex) amplitude $T(S)$. It is shown in Section 3 of I that the eigenvalues $S_j(K_0)$ depend on the phase $\mu(S)$ and the modulus $|T(S)|$ of $T(S)$ according to the equation

$$|T(S)| \cos K_0 a = \cos\left(a(K_c^2 + S)^{1/2} + \mu(S)\right), \quad (5.9)$$

which results from matching the waves scattered by the barriers, using the Bloch condition (5.5).

The condition (5.9) (which has been derived several times before[1,10]) is precisely equivalent to the determinantal equation (5.8), but it is more transparent. As S increases through zero, $|T(S)|$ rises rapidly from zero to unity, and the Bloch waves change their nature from being "tightly bound" to "nearly free". This is the quantum-mechanical analogue of the division of classical paths into bound and nearly free which we have discussed in Section 3. To proceed further we employ the well-established WKB approximation (see Sections 1–4 of II) for barrier penetration. When applied to the present problem (see Section 4 of I), the method shows that $|T(S)|$ depends on the "barrier integral" $q(S)$, defined as

$$q(S) \equiv \int_{-x_t^+(S)}^{x_t^+(S)} (\bar{U}(S) - S)^{1/2}\, dx, \quad (5.10)$$

where $x_t^+(S)$ is the classical turning-point lying between 0 and $a/2$ for $S < 0$, which was introduced in Section 3. When $S > 0$, Eq. (5.10) still holds, but now $x_t^+(S)$ is imaginary, and $q(S)$ is negative. In terms of $q(S)$, $|T(S)|$ is given approximately by

$$|T(S)| \approx (1 + e^{2q(S)})^{-1/2}, \quad (5.11)$$

which, as expected, rises rapidly from 0 to 1 as S increases through zero. The phase $\mu(S)$ of $T(S)$ depends on the "phase integral" $\phi(S)$ given by the classical action integral across the potential well between adjacent barriers and it is found that

$$\left.\begin{aligned} a(K_c^2 + S)^{1/2} + \mu(S) &\approx \phi(S) \\ &= \int_{x_t^+(S)}^{a - x_t^+(S)} (S - \bar{U}(x))^{1/2}\, dx \quad (S < 0) \\ &= \int_0^a (S - \bar{U}(x))^{1/2}\, dx \quad (S > 0) \end{aligned}\right\}. \quad (5.12)$$

Thus ϕ increases monotonically from zero at $S = -K_c^2$.

The approximations (5.11) and (5.12) lead to a simple graphical method for solving the eigenvalue equation (5.9). Figure 19 shows curves of $|T| \cos K_0 a$ and $\cos\phi$ vs. S. The intersections occur at the eigenvalues $S_j(K_0)$. Variation of K_0 changes the curve $|T| \cos K_0 a$, and hence the eigenvalues. But when S is below the region near the barrier top, $|T|$ is so small

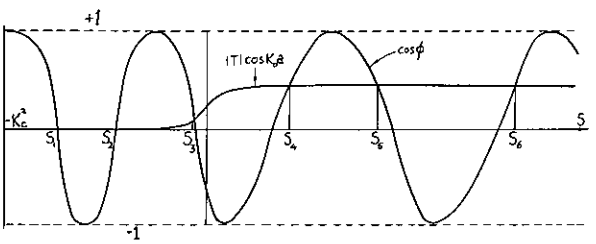

FIGURE 19 Graphical construction for eigenvalues $S_j(K_0)$.

that varying K_0 has little effect on the eigenvalues, which therefore correspond to "flat" branches of the dispersion surface. These "tight-bound energy bands" are located at values of S_j satisfying

$$\phi(S_j) = (j + \tfrac{1}{2})\pi, \quad (5.13)$$

which is precisely the WKB condition for bound states of the potential well associated with each atomic plane. Above the region near the barrier top, $|T|$ is almost unity, and the roots of Eq. (5.9) sweep through almost

all values of S as K_0 varies from 0 to π/a; the corresponding "nearly-free" Bloch states lie in broad "energy" bands separated by narrow gaps.

When will this picture given by the WKB method be valid? The "official" condition for the applicability of asymptotic ("semiclassical") techniques is that the potential must vary slowly in comparison with the wave function.[11] This would be true for the large values of j in Figure 19 or Eq. (5.13). However, wide experience suggests that the WKB method provides good numerical approximations even for the lowest eigenvalues. The present problem is no exception, as Figure 20 shows. This is a comparison of the dispersion surface calculated using the WKB approximation (Eqs.

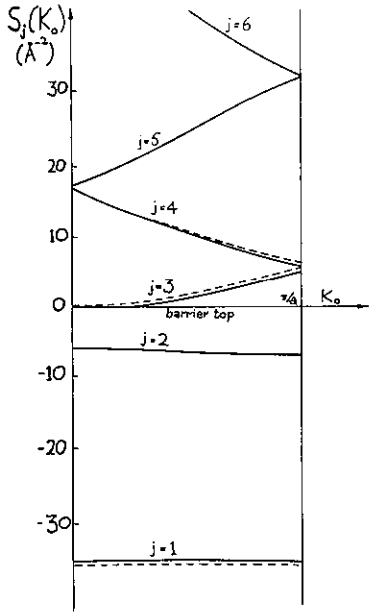

FIGURE 20 Comparison of WKB approximation (– – – –) with 17 beam calculation (————) of Bloch eigenvalues for Gold (111) at 600 kV. (The occurrence of an eigenvalue close to $S = 0$ for $K_0 = 0$ is fortuitous.) Courtesy of Dr. A. C. Enfield.

(5.9), (5.12), (5.13)) with the "exact" surface calculated from Eq. (5.8) truncated to a 17 x 17 determinant (a so-called "17-beam" calculation). We have chosen as example the case of Gold (111) at 600 kV, for which a micrograph is shown as Figure 14. It is clear that the semiclassical method works rather well for all branches j. There is a slight discrepancy for the lowest state, which arises because the region near the bottom of the potential well is a rounded-off cusp instead of being simply parabolic. There are also small discrepancies near the barrer top, which arise from neglecting a small "wiggle" in the phase $\phi(S)$ which modifies Eq. (5.12) in that region (see Sections 3.3 and 4.2 of II). We have also neglected a small modification in the transmission coefficient $|T(S)|$ just above $S = 0$ to which we shall return in Section 7 when we discuss the critical voltage effect. Figure 20 shows the clear distinction between "tightly bound" and "nearly free" states which is ultimately classical in its origin; it is surprising that this distinction is quite sharp even for a potential so weak that it binds only two states.

This real-space method for understanding the dispersion surface may be generalized to deal with the two-dimensional "cross-grating" case, although many details have yet to be explored. Instead of the reflection and transmission coefficients for backward and forward scattering from planes, we introduce the *phase shifts* $\eta_l(S)$ for the scattering from an atomic string of the partial wave with angular momentum l at "energy" S. Equation (5.9) then becomes the KKR determinantal condition of band theory,[12] namely

$$\left.\begin{aligned} &\det_{ll'} \|(\cot \eta_l(S) - i)\delta_{ll'} \\ &\qquad + B_{l-l'}(S, \mathbf{K}_0)\| = 0 \\ &B_m(S, \mathbf{K}_0) \equiv \sum_{i \neq 0} e^{i\mathbf{K}_0 \cdot \mathbf{R}_i + im\phi_i} \\ &\qquad \times H_m^{(1)}(S^{1/2} R_i) \end{aligned}\right\}, \tag{5.14}$$

where $H_m^{(1)}$ is the Hankel function of the first kind and $\mathbf{R}_i (= R_i, \phi_i)$ are the sites on which strings are centred. This formalism brings out the distinction between bound and free states; in particular, when $S < 0$ the "structure constants" B_m are very small, and (5.14) shows that the eigenvalues satisfy

$$\cot \eta_l(S) = i, \tag{5.15}$$

which is precisely the condition for a bound state in the single-string potential $\bar{U}(|\mathbf{R}|)$, and which does not involve $\mathbf{K}_0$ and thus corresponds to "flat" branches $S_j(\mathbf{K}_0)$.

The basic quantum-mechanical expression (5.6) for the diffraction amplitudes $A_G(z, \mathbf{K}_0)$ contains integrals over the Bloch waves, as well as the eigenvalues we have been discussing. The semiclassical method provides an analysis of these integrals, as elaborated for the one-dimensional case in Section 4 of I. In outline, the procedure is as follows: the WKB method gives formulae for the eigenfunctions $\tau_j(\mathbf{R})$ which are oscillatory in classically allowed regions ($S > \bar{U}(\mathbf{R})$) and exponentially damped into classically forbidden regions ($S < \bar{U}(\mathbf{R})$). These regions are separated by classical turning points (or lines in two dimensions) where $S = \bar{U}(\mathbf{R})$. At such turning points (which can only exist for bound states, since $\bar{U}(\mathbf{R})$ is negative) the

WKB method breaks down and predicts infinite values for $\tau_j(\mathbf{R})$. This is not such a disaster as it seems, because the false singularities are integrable, and hardly affect the values of the integrals in (5.6).

As a numerical technique for finding $A_G(z, \mathbf{K}_0)$ this is probably satisfactory, but it is possible to go further, and approximate the integrals *analytically*, using the principle of stationary phase to extract the main contributions from the oscillating integrands. This immediately suggests that any Bloch state j for which either integrand in (5.6) contains no stationary points (for any value of $\mathbf{R}$) does not contribute significantly to $A_G(z, \mathbf{K}_0)$. When the analysis is carried through, the remarkable result emerges that the only Bloch waves contributing to the first integral in (5.6) are those for which S_j lies in the band (3.2) containing the energies S of all the *classical paths* of electrons entering with direction $\mathbf{K}_0$. The Bloch waves contributing to the second integral in (5.6) lie in a similar band with $\mathbf{K}_0$ replaced by $\mathbf{K}_G$. Only those states lying in the overlap of these two bands contribute to $A_G(z, \mathbf{K}_0)$.

For the undiffracted beam ($\mathbf{G} = 0$) the bands of contributing S-values coincide, and if, in addition, the electrons hit the crystal normally ($\mathbf{K}_0 = 0$), these bands include just the "bound" states of $\bar{U}(R)$. The total number of these states gives the number $N(E)$ of terms contributing to the Bloch wave series (5.6) at energy E, and hence a measure of the convergence of the series. For the planar case, (5.13) gives

$$N(E) = \frac{\phi(0)}{\pi} = \frac{1}{\pi}\int_0^a (-\bar{U}(x))^{1/2}\,dx, \qquad (5.16)$$

while a similar analysis for the cross-grating case gives

$$N(E) = \tfrac{1}{2}\int_0^\infty |\bar{U}(R)|R\,dR, \qquad (5.17)$$

where $\bar{U}(R)$ is the potential on one of the superposed atomic strings (assumed cylindrically symmetric). The potential depends on the relativistic mass via Eqs. (1.4) and (1.5), so that $N(E)$ increases with E, faster for the cross-grating case than for the planar case, and the Bloch wave series converges more slowly as E increases.

For sufficiently large $|\mathbf{G}|$, there is no overlap between the bands of S_j-values contributing to the integrals in (5.6), so that diffracted beams with these $\mathbf{G}$-values are not expected to appear with significant intensity. The analysis shows that the "fan" of significant diffracted beams lies between $G_{\min}$ and $G_{\max}$, given by the *classical* results (3.4)-(3.6) and shown in Figure 8.

It thus appears that the bands of contributing eigenvalues, and the limits of the fan of diffracted beams, can be predicted on the basis of classical mechanics, even within the wave theory! How reliable are these results? Clearly they are approximations, which we cannot expect to be as good as the WKB eigenvalues (cf. Figure 20), since the additional stationary-phase approximation has been made; the integrals in (5.6) will not vanish for Bloch waves outside the bands we have described, but will merely take on small values. Nevertheless, the values found for $N(E)$, $G_{\min}$ and $G_{\max}$, can be expected to be more accurate as E increases, becoming exact in the asymptotic limit, when $N(E)$ becomes infinite.

In this limit, however, the Bloch wave series (5.6) is useless, because it contains an infinite number of significant terms. To conclude this section, we explain in outline how the series may be transformed into the "interfering classical path" series (2.2). In physical terms, what happens is that most of the large number of contributing terms in the Bloch wave series cancel by mutual interference; the exceptions are certain groups of terms which are mutually coherent. These lie near to those values of S, (depending on z, $\mathbf{K}_0$ and $\mathbf{K}_G$) which correspond to the "energies of classical paths contributing to the diffracted beam as explained in Sections 2-4. Mathematically, the tool for dealing with such series is the *Poisson summation formula*, namely

$$\sum_{j=-\infty}^{\infty} f_j = \sum_{m=-\infty}^{\infty}\int_{-\infty}^{\infty} df_j\, e^{2\pi imj}, \qquad (5.18)$$

This is applied to the Bloch wave series (5.6) and the resulting integrals are evaluated approximately by the method of stationary phase. It turns out to be simpler to integrate over S_j rather than j—the details can be found in Section 5 of I. When this procedure is carried out, the series (2.2) results, and the new summation index m labels precisely the "families of contributing classical paths" discussed in Sections 3 and 4. Thus each classical path is a "wave packet" made up of a group of neighbouring Bloch waves which happen to be coherent at the particular z, $\mathbf{K}_0$ and $\mathbf{K}_G$ considered.

Just which of the various approximations should be used in any particular case depends on what one is interested in, as well as on the energy E. What follows is a guide rather than a set of hard-and-fast rules. For eigenvalues, the WKB method is good when $N(E)$ exceeds about 1.5. In the planar case, this occurs at several hundred kV for light elements, while for heavier elements the approximation is valid down to much lower voltages. When $N(E) < 1.5$ the determinantal method is simpler (generally at least a $2N \times 2N$ determinant must be used to ensure convergence). At

low energies two simple analytic approximations can often be used[3]: in the first, (5.8) is approximated by a 2 x 2 determinant and the resulting quadratic equation solved explicitly; this is the "two-beam" case. In the second case, the potential coefficients U_G are so small that the dispersion surface differs only by a small perturbation from the free-electron case (there is only one "bound band", so near to $S = 0$ that barrier penetration causes considerable curvature in $S_1(\mathbf{K}_0)$); this is the "Born approximation" or "Kinematic" case, much employed in x-ray diffraction. In the *cross-grating case* these two approximations rarely apply; $N(E)$ is large, and the states contributing to (5.17) range over various angular momenta from 0 to l_{max}, which is therefore less than $N(E)$. Thus the KKR determinant (5.14) is always smaller than the reciprocal-lattice determinant (5.8) (for Tungsten at 750 kV, N is 36 while l_{max} is 5).

For accurate computations of diffraction amplitudes the Bloch wave series is probably better than the classical path series—at least for currently-attainable voltages. So far as semiclassical techniques are concerned, it is probably better to use WKB Bloch functions and compute the integrals in (5.6), rather than use the stationary-phase method. However, to explain the patterns of lines and spots on micrographs, the approach explained in Sections 2–4, based on caustics and interference fringes, is remarkably effective, even when N is only 2 or 3.

6 PHENOMENOLOGICAL INCLUSION OF ABSORPTION—ANOMALOUS TRANSMISSION FOR ELECTRONS

The basic theoretical model we have been using, of noninteracting electrons propagating elastically in a static crystal potential $V(\mathbf{r})$, gives a good zero-order description of diffraction contrast effects. However, the real situation is much more complicated than this: *inelastic processes* can occur, such as interaction with thermal vibrations, excitation of core electrons, and production of plasmons. One effect of these processes is to break the strict periodic symmetry of the interactions, so that emerging electrons are no longer restricted to the directions $\mathbf{K}_G$ defined in (1.1). A full description of the angular distribution of inelastically scattered electrons is difficult, but it is clear that their existence must result in a reduction of the intensity of the beams diffracted into directions $\mathbf{K}_G$; this reduction is called *absorption*. If the focal-plane aperture (Figure 1) in a diffraction contrast experiment is small enough, most of the inelastically scattered electrons will be excluded, so that the basic problem remains the calculation of elastic diffraction amplitudes $A_G(z, \mathbf{K}_0)$, but now absorption effects must be considered. Thus the images we are considering differ fundamentally from the "star" patterns of heavy-particle channelling which are formed by the directional distribution of *all* scattered particles, and are thus dominated by inelastic effects; their electron analogues are *Kikuchi patterns*.[2,3]

It is well known[13,14] that the effect of absorption on the elastic diffraction amplitudes may be included phenomenologically by adding a *small imaginary part* to the potential $V(\mathbf{r})$. This procedure is valid if the inelastic interactions may be considered as a first-order perturbation of the elastic interactions. Thus the projected potential $\bar{U}(\mathbf{R})$ defined by (1.4) must be replaced by

$$\bar{U}(\mathbf{R}) \to \bar{U}^r(\mathbf{R}) + i\bar{U}^i(\mathbf{R}), \tag{6.1}$$

where the notation is obvious. $\bar{U}^i(R)$ is a small negative function whose magnitude is greatest at the atomic strings or planes, since inelastic interactions are most likely to occur near the atoms. The real $\bar{U}^r(R)$ closely resembles the perfect-crystal elastic potential; the slight modifications introduced by inelastic effects amount to a smearing-out of the projections of the Coulomb singularities at the atoms (in the "planar case", Figure 7 replaces Figure 2).

Let us first consider the effect of this complex potential on the *Bloch wave theory*, using the semiclassical results of Section 5. Only a brief account will be given, since a fuller treatment appears elsewhere.[15] To first order the most important effect of $\bar{U}^i(R)$ is to add a small imaginary part to the Bloch eigenvalues S_j, i.e.

$$S_j \to S_j^r + iS_j^i, \tag{6.2}$$

where, from perturbation theory

$$S_j^i \approx \iint_{\text{cell}} d\mathbf{R} |\tau_j(\mathbf{R})|^2 \bar{U}^i(\mathbf{R}) \tag{6.3}$$

and we have used the fact that $\tau_j(\mathbf{R})$ is normalized. Thus S_j^i is always *negative*. The first-order correction to $\tau_j(\mathbf{R})$ itself is relatively unimportant and will be neglected. The imaginary part of the eigenvalue, S_j^i, describes *selective absorption of the Bloch waves*, because in the series for $A_G(z, \mathbf{K}_0)$ (Eq. (5.6)) it leads to the replacement

$$e^{-iS_j(\mathbf{K}_0)z/2k} \to e^{-iS_j^r(\mathbf{K}_0)z/2k}\, e^{-|S_j^i(\mathbf{K}_0)|z/2k}. \tag{6.4}$$

For small thickness z the exponential damping factors have little effect on the diffraction contrast, and the contributing Bloch waves may be identified as explained in Section 5. But for thick specimens the

absorption is a dominant effect, and Eq. (6.4) shows that it is only the Bloch wave m, where $|S_m{}^i(\mathbf{K}_0)|$ is the smallest member of the set $|S_j{}^i(\mathbf{K}_0)|$, which survives the inelastic scattering, and remains exponentially larger than the other Bloch waves. Then the diffraction intensity (5.6) becomes

$$|A_G(z, \mathbf{K}_0)|^2 \underset{z\to\infty}{\longrightarrow} \left| \iint_{\text{cell}} d\mathbf{R}\tau_m{}^*(\mathbf{R})\, e^{i\mathbf{K}_0\cdot\mathbf{R}} \times \iint_{\text{cell}} d\mathbf{R}\tau_m(\mathbf{R})\, e^{-i\mathbf{K}_G\cdot\mathbf{R}} \right|^2 \times e^{-|S_m{}^i(\mathbf{K}_0)|z/k}. \tag{6.5}$$

A simple measure of the *penetration depth* d which can be achieved using diffraction contrast techniques at any given energy E and orientation $\mathbf{K}_0$ is given by

$$\frac{1}{d} \equiv \frac{S_m{}^i(\mathbf{K}_0, E)}{k(E)}. \tag{6.6}$$

It is, therefore, important to understand on the basis of Eq. (6.3) just how $S_j{}^i$ varies among the Bloch waves j, for varying $\mathbf{K}_0$ and E. To obtain this understanding, we restrict ourselves to the one-dimensional (planar) case, and use WKB approximations for the eigenfunctions $\tau_j(x)$ (see Section 4 of I). This leads[15] to the following simple formula:

$$S_j{}^i(S_j{}^r) = \frac{\operatorname{Re} \int_0^{a/2} dx \bar{U}^i(x)(S_j{}^r - \bar{U}^r(x))^{-1/2}}{\operatorname{Re} \int_0^{a/2} dx (S_j{}^r - \bar{U}^r(x))^{-1/2}}. \tag{6.7}$$

The "real part" notation is a device for ensuring that when $S_j{}^r < 0$ only classically accessible regions contribute to the integrals.

We can immediately draw an important qualitative conclusion from (6.7): when $S_j{}^r > 0$ the integrand is a smooth function of x, and $S_j{}^i$ has a certain negative value, but when $S_j{}^r < 0$ (bound states) the integrand is dominated by the turning point $x_t{}^+(S_j{}^r)$, so that the value $\bar{U}^i(x_t{}^+)$ plays a principal role in determining $S_j{}^i$. Now, as $S_j{}^r$ increases towards zero, $x_t{}^+$ moves towards the barrier top, where $|U^i(x)|$ is smallest. Therefore, the smallest value of $|S_j{}^i|$ occurs for the Bloch state whose "energy" $S_j{}^r$ lies nearest the barrier top. It is near the barrier top that the Bloch functions $\tau_j(x)$ are most concentrated between the atomic planes, and the principle that such states (which avoid much of the strong inelastic scattering at the atoms) are least absorbed is known as "Bloch wave channelling" or "anomalous transmission;[3] what we are discussing is the electron analogue of the "Borrmann effect"[16] for x-rays.

A quantitative test of Eq. 6.7 is shown in Figure 21:

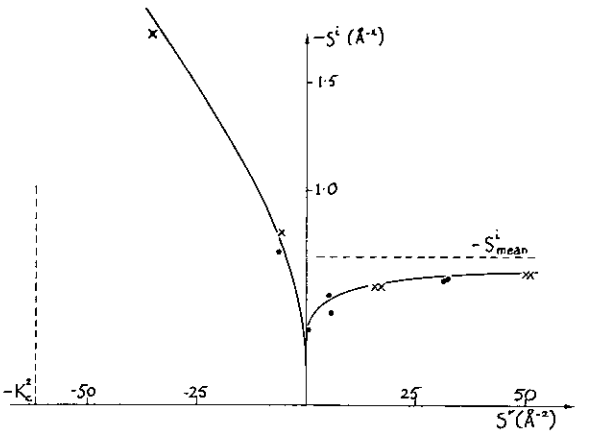

FIGURE 21 Imaginary part of eigenvalue vs. real part for gold (111) at 600 kV. ———— semiclassical theory, x exact calculation, $K_0 = 0$, • exact calculation, $K_0 = \pi/a$.

for the case of gold (111) at 600 kV, we have plotted S^i vs. S^r, as predicted by Eq. (6.7) (full line), and from 21 x 21 determinant calculations with $K_0 = 0$ (crosses) and $K_0 = \pi/a$ (dots). The agreement is good. When S^r becomes very large, S^i tends to the "mean absorption", namely,

$$S^i \underset{S^r\to\infty}{\longrightarrow} S^i{}_{\text{mean}} \equiv \frac{1}{a}\int_0^a dx \bar{U}^i(x). \tag{6.8}$$

To achieve maximum penetration, then, it is necessary to excite states near the barrier top. A semiclassical analysis[15] shows that states with $S_j{}^r \approx 0$ are most strongly excited when $K_0 = G = 0$—i.e. in bright field at normal incidence. This still leaves the electron energy E as a free variable, which should obviously be chosen to minimize the quantity $1/d$ defined in Eq. (6.6). The presence of the factor $k(E)$ indicates that the minimum will not quite lie at the minimum of S^i (i.e. for states with $S^r = 0$) but will occur for states which are slightly bound. The quantity $1/d$ is plotted on Figure 22 as a function of E (with $K_0 = 0$) from Eqs. (6.6) and (6.7), and compared with another estimate of the penetration based on a full many-wave calculation.[17] Both curves predict a maximum of penetration, at almost identical voltages near 900 kV, so that the semiclassical method provides a simple method for discovering how to maximize penetration using diffraction contrast.

At the normal incidence which the method requires, only symmetric Bloch waves j are excited; in Figure 22

for example, it is the symmetric Bloch wave 3 (cf. Figure 20) which lies near the barrier top. As the energy increases, the potential $\bar{U}(x)$ will become stronger because of relativistic effects (Eqs. (1.4),

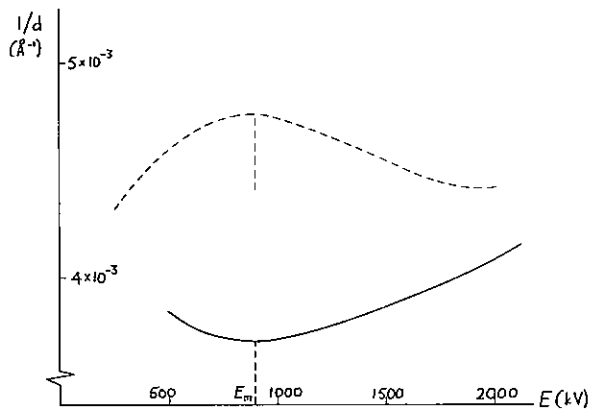

FIGURE 22 Comparison of inverse penetration depth (————) with Humphreys[17] many-beam calculations of penetration (- - - - - - arbitrary units) for gold (111).

(1.5)), and more states will be bound. Thus there will be a *series* of penetration maxima, near the energies E at which new symmetric states are sucked down through the barrier top $S^r = 0$. For gold (111) the second maximum ($j = 5$) occurs when E is about 4 MeV, and could not be observed with existing microscopes.

We conclude this section by studying the effect of the imaginary potential $\bar{U}^i(x)$ on the *classical path theory* of Sections 2–4. As explained in Section 5, the transformation from the Bloch wave series (5.6) to the interfering classical path series (2.2) is made with the aid of the Poisson summation formula (5.18). When the absorption factor (6.4) is incorporated into the Bloch waves, the analysis proceeds in exactly the same way, with the result that each contributing classical path in (2.2) is weighted with the amplitude factor $\exp(-z|S^i(S)|/2k)$, where $S^i(S)$ is given by (6.7) and S is the "energy" of the classical path, and depends on K_0, K_G and z. Thus the purely classical *intensity*, in which all phase effects are ignored, is given not by (2.13) but by

$$|A_G(z, \mathbf{K}_0)|^2 \approx C^2 \sum_i \rho_i(\mathbf{K}_0, \mathbf{K}_G, z) \times e^{-z|S^i(S_i(\mathbf{K}_0, \mathbf{K}_G, z))|/k}. \qquad (6.9)$$

To interpret the exponent in this equation, we recall the classical path equations (2.6), (3.7) and (3.9), which enable us to write, using (6.7), to a good approximation

$$\frac{z}{k} S^i(S) = \frac{z}{k} \operatorname{Re} \int_0^{a/2} \frac{dx \bar{U}^i(x)}{(S - \bar{U}^r(x))^{1/2}} \Big/ \operatorname{Re} \int_0^{a/2} \frac{dx}{(S - \bar{U}^r(x))^{1/2}}$$

$$\approx \frac{z}{k} \frac{\int_0^z dz' \bar{U}^i(x(z'))}{\int_0^z dz'}$$

$$= \int_0^z dz' \bar{U}^i(x(z'))/k, \qquad (6.10)$$

where $x(z')$ is the equation of the classical path being considered. When this is inserted into Eq. (6.9) it is immediately evident that $|\bar{U}^i(x)|/k$ is the *inverse mean free path* for scattering of an electron out of a classical path in the real potential $\bar{U}^r(x)$; thus $\bar{U}^i$ is closely related to the "stopping power" of channelling theory.[4] Obviously, the mean free path is position-dependent, and this accounts for the "path-integral" form of (6.10). For thick specimens, the only important classical paths in the series (6.9) are those which are least absorbed, and it is obvious that these are the paths which avoid the atomic planes (or strings in the cross grating case) as much as possible.

7 INTO THE HEART OF THE WAVE THEORY—THE CRITICAL VOLTAGE EFFECT

In this section we demonstrate the full power of the semiclassical method by developing a theory for the most delicate wave effect which has so far been discovered in diffraction contrast microscopy. The dispersion surfaces for the Bloch eigenvalues $S_j(\mathbf{K}_0)$ corresponding to nearly-free states are generally separated by very small "energy" gaps in the Bragg directions $\mathbf{K}_0 = \mathbf{G}/2$; this can be seen in Figure 20, for example. The form of the dispersion surfaces changes with the electron energy E, and it often happens that at certain "critical voltages" $E_c^{(n)}$ the Bloch states n and $n + 1$ become "accidentally degenerate"—i.e. their dispersion surfaces touch and S_n equals S_{n+1}. This can have a dramatic effect on observed thickness fringes;[18] to see this, we note from Eq. (5.6) that the fringes arise from various Bloch waves beating together and the fringe spacing resulting from waves n and $n + 1$ is proportional to $(S_{n+1} - S_n)^{-1}$. As E passes through $E_c^{(n)}$ this spacing becomes infinite, and this set of fringes

disappears. Of course, Bloch waves n and $n+1$ must be significantly and comparable excited for this disappearance to be observable, but this can be achieved by an appropriate choice of $\mathbf{K}_0$ and $\mathbf{G}$, and critical voltages are currently being measured to an accuracy of ±10 kV.[18]

As well as providing very accurate predictions of $E_c^{(n)}$ for the case of diffraction by atomic planes, the semiclassical theory also explains the subtle changes of symmetry and excitation of the Bloch waves near critical conditions. In this review we shall not deal with these latter aspects, because the theory is complicated and a full account will be published later.[19] To see how it is possible for two eigenvalues to degenerate, we recall the exact formula (5.9) for $S_j(K_0)$, the WKB approximation (5.12) for the phase, and the graphical construction shown in Figure 19. For degeneracy, the curves on Figure 19 must touch at some value of S (i.e. two intersections must coincide). Since $\phi(S)$ is monotonic, this can only occur when

$$\cos\phi(S) = |T(S)|\cos K_0 a = \pm 1. \tag{7.1}$$

Now $|T(S)|$ can never exceed unity, so that to satisfy (7.1) $|\cos K_0 a|$ must be unity–i.e. K_0 must be a Bragg direction $m\pi/a$, where m is any integer–and $|T(S)|$ must actually attain the value unity–i.e. the reflection coefficient $R(S)$ from the interatomic potential barrier must vanish. At a critical voltage, therefore, the following conditions must be simultaneously satisfied:

$$\left.\begin{aligned} &\phi(S) = n\pi \quad (n = 1, 2, 3\ldots)\\ &R(S) = 0\\ &K_0 = \text{even Bragg direction for even } n\\ &\quad = \text{odd Bragg direction for odd } n \end{aligned}\right\} \cdot (7.2)$$

The WKB approximation for $|T(S)|$, Eq. (5.11), never attains the value unity for finite S (although it is very close to unity above the region of the barrier top); therefore $R(S)$ is never zero, and no critical voltages are predicted, although as Figure 20 shows the method does give a good overall description of the dispersion surface. The reason for the failure of (5.11) is its neglect of all reflections other than those arising from the neighbourhood of the parabolic barrier top. But there will also be reflected waves from the non-analyticity of the barrier $\bar{U}(x)$ at the atomic planes (in Figure 18 the curvature vanishes abruptly at $\pm a/2$). For certain values of S these reflections may interfere destructively with those from the barrier top, so that R is zero and $|T|$ unity. This behaviour of R and $|T|$ is analogous to the Ramsauer–Townsend effect[20] in atomic scattering, and the graphical explanation of the critical voltage effect which it implies[21] is shown in Figure 23.

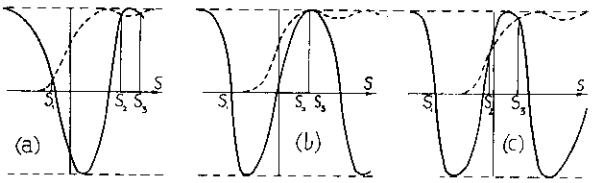

FIGURE 23 Curves of $\cos\phi(S)$ (———) and $|T(S)|$ (-----) for (a) $E < E_c^{(2)}$ (b) $E = E_c^{(2)}$ (c) $E > E_c^{(2)}$.

The "ripples" in $|T(S)|$ always occur above the barrier top, and since it can be shown that the lowest state $j = 1$ is always bound, no matter how weak $\bar{U}(x)$ may be, this implies that no "first-order" critical voltages ($n = 1$ in (7.2)) can occur. To find the higher $E_c^{(n)}$, an accurate formula for $R(S)$ is required. This may be found by replacing the barrier in Figure 18 by a "staircase" of tiny discontinuities and considering just the first-order reflection from each step (see Section 2.2 of II). The result is

$$R(S) \approx \frac{1}{4}\int_{-a/2}^{a/2} dx\, \frac{d\bar{U}(x)/dx}{S - \bar{U}(x)}\, e^{2i\int_0^x dx'(S-\bar{U}(x'))^{1/2}/\hbar}, \tag{7.3}$$

a formula originally presented by Landauer[22] in 1951, who also considered periodic potentials and presciently realized that degeneracies could occur. Unlike the WKB formula (5.11), which is valid for all S, (7.3) holds only above the barrier region, but this is precisely the region involved in the critical voltage effect.

Now we introduce a relativistic scaling technique based on (1.4) and (1.5) to enable calculations for different energies E to be carried out using potentials, etc, for $E = 0$. We define

$$\left.\begin{aligned} \bar{U}_0(x) &\equiv \frac{m_0}{m(E)}\bar{U}(x)\\ S_0 &\equiv \frac{m_0}{m(E)}S\\ \phi_0(S_0) &\equiv \int_{-a/2}^{a/2} dx(S_0 - \bar{U}_0(x))^{1/2}\\ &= \left(\frac{m_0}{m(E)}\right)^{1/2}\phi(S) \end{aligned}\right\} \tag{7.4}$$

Then the critical voltage equations (7.2) take the simple form

$$E_c^{(n)} = m_0c^2\left[\left(\frac{n\pi}{\phi_0(S_0)}\right)^2 - 1\right], \tag{7.5}$$

where S_0 is the solution of

$$\int_0^{a/2} dx \frac{d\bar{U}_0(x)}{dx} \frac{1}{S_0 - \bar{U}_0(x)} \sin\left[\frac{2n\pi}{\phi_0(S_0)} \int_0^x dx' \times (S_0 - \bar{U}_0(x'))^{1/2}\right] = 0 \qquad (7.6)$$

(the symmetry of the barrier about $x = 0$ has been used). Numerical evaluation of the left-hand member of (7.6) for various positive S_0 is very simple, and any zeros immediately give critical voltages from (7.5).

This semiclassical formalism based on Landauer's expression (7.3) for the reflection coefficient is strictly valid in the asymptotic limit when $\phi(S)$ and hence the order n of $E_c^{(n)}$ becomes infinite. But it gives astonishingly accurate results even for the practical cases of $n = 2$–6, for which most critical voltages lie below a few MeV. This is shown in table (II) for the case of a

TABLE II
Comparison of exact (determinantal) and semiclassical critical voltages (temperature 293 K)

Element reflection	n	$E_c^{(n)}$ exact (kV)	$E_c^{(n)}$ semiclassical (kV)
Al 200	2	995	963
	4	4335	4325
	5	5460	5488
		7970	7882
	6	5010	5021
Au 200	2	105	76.1
	4	1755	1739
	5	1640	1649
		3700	3655
	6	1380	1373

light element (Al) and a heavy element (Au). These are representatives of about fifty critical voltages which have been calculated, the average error being about 1.5%. As expected, the accuracy increases with n. The "exact" computations based on the determinant (5.8) are difficult, because matrix diagonalization techniques often fail precisely where two eigenvalues degenerate; also, it is prohibitively expensive in computer time to search the whole voltage range, so the semiclassical values are used as a starting point. No 3rd order critical voltage has been found for cases where the potential barrier has the form of Figure 18, and indeed a consideration of the factors in the integrand of (7.6) suggests that a zero is extremely unlikely when $n = 3$. It is found that $E_c^{(n)}$ is very sensitive to temperature[18] –i.e. to the form of the potential well near $\pm a/2$ (Figure 18); indeed, the two pairs of 5th order critical voltages in table II approach, coalesce and disappear as the temperature is reduced, and this corresponds to a higher-order degeneracy of the Bloch waves.

Rather surprisingly, it is possible–at least to a good approximation–to take advantage of the sensitivity of $E_c^{(n)}$ to $\bar{U}(x)$ and the simplicity of the semiclassical equations (7.5) and (7.6), and devise an inversion technique to actually obtain $\bar{U}(x)$ from $E_c^{(n)}$. Introducing the obvious new variable.

$$\psi(x) \equiv \frac{2\pi}{\phi_0(S_0)} \int_0^x dx'(S_0 - \bar{U}_0(x))^{1/2}, \qquad (7.7)$$

Eq. (7.6) becomes

$$\int_0^{\pi} d\psi f(\psi) \sin n\psi = 0, \qquad (7.8)$$

where a little algebra shows that

$$f(\psi) = -2 \frac{d}{d\psi} \ln\left(\frac{dx}{d\psi}\right). \qquad (7.9)$$

If $f(\psi)$ is known, solution of this equation gives the original variable x as

$$x(\psi) = \frac{a \int_0^{\psi} d\psi' \, e^{-1/2 \int_0^{\psi'} d\psi'' f(\psi'')}}{2 \int_0^{\pi} d\psi' \, e^{-1/2 \int_0^{\psi'} d\psi'' f(\psi'')}} \qquad (7.10)$$

while inversion of (7.7) using (7.5) gives the potential as

$$\bar{U}_0(x) = \left[\frac{1}{a} \int_0^{\pi} d\psi \, e^{-1/2 \int_0^{\psi} d\psi' f(\psi')}\right]^2 \times \frac{m_0 c^2 n^2}{(E_c^{(n)} + m_0 c^2)} (1 - e^{\int_0^{\psi(x)} d\psi f(\psi)}). \qquad (7.11)$$

But how can we find $f(\psi)$, the function on which the inversion depends? Analysis of (7.7) and (7.9) shows that $f(\psi)$ is an odd function of period 2π, so that we may write

$$f(\psi) = \sum_{m=1}^{\infty} A_m \sin m\psi, \qquad (7.12)$$

and (7.8) tells us that A_n vanishes. The grossest approximation is to neglect all $A_{m>1}$; for $E_c^{(2)}$, A_2 vanishes anyway, so we are effectively ignoring A_3, A_4 . . . . Then (7.10) and (7.11) give $\bar{U}_0(x)$ as a

function of the single parameter A_1. We find A_1 by fitting exactly the minimum value $\bar{U}(a/2)$, which can be obtained experimentally from the "critical direction' K_c using Eq. (3.3) (cf. Figure 8). Figure 24 shows two

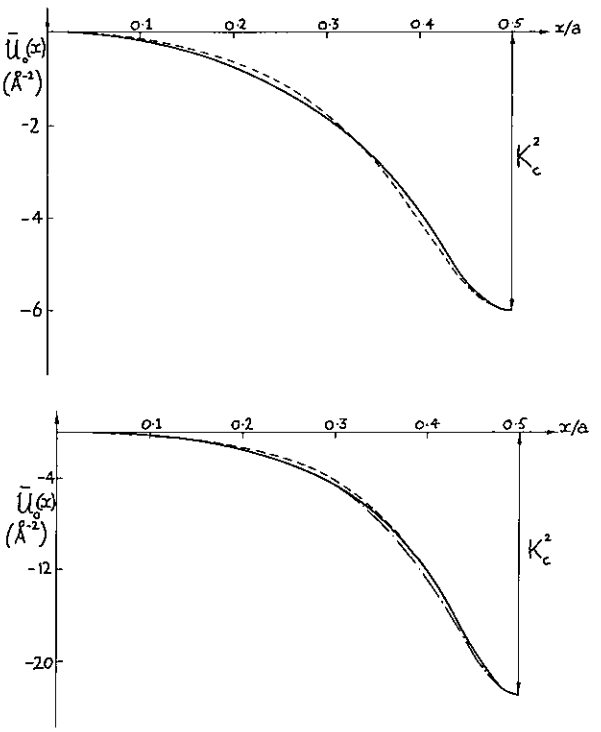

FIGURE 24 Comparison of exact (————) and reconstructed (– – – – –) potentials for (a) Al (200) at 293K, (b) Au (200) at 293K using $E_c^{(2)}$. The line (– · – · – · –) on (b) is the reconstruction from $E_c^{(4)}$.

potentials $\bar{U}_0(x)$ which have been "reconstructed" in this way. Starting from a given "exact" potential, K_c^2 is read off and $E_c^{(2)}$ computed using exact determinantal methods; then (7.11) and (7.12) are used. In terms of the Fourier coefficients of the potential, the reconstructions are accurate to about 2%. Thus this simple method, based on just two measurable quantities $E_c^{(2)}$ and K, rivals full many-beam computer simulations of bend contours;[23] however, it must be stated that the accuracy with which K_c can be measured has yet to be investigated.

In more complicated crystal structures the diffracting planes may not always be equally spaced, and the potential $\bar{U}_0(x)$ may not have the same form as Figure 24. The case of Silicon (111) is particularly interesting:[24] no longer does (7.6) prohibit 3rd order critical voltages, and indeed there is one, at 1145 kV for 293K, while the semiclassical method predicts 1109 kV; there is also a 5th order critical voltage, at 1595 kV, a value predicted exactly by the semiclassical method! To reconstruct such more complicated potential profiles, it is not sufficient to retain just A_1 in (7.12), but A_2 as well. Then two properties of $\bar{U}_0(x)$ must be fitted, and we have again taken the potential minimum (i.e. $-K_c^2$), and also assumed that this occurs exactly at the known position of the atomic planes. The result is shown in Figure 25.

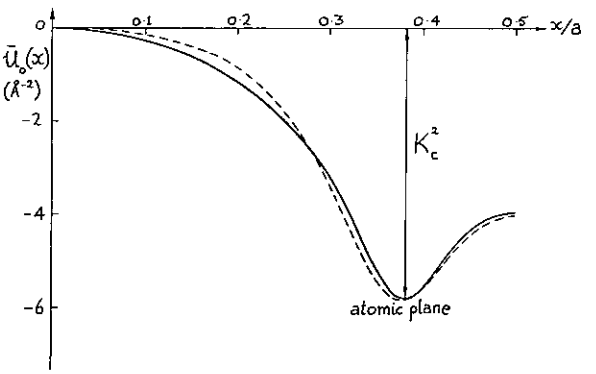

FIGURE 25 Comparison of exact (————) and reconstructed (– – – – –) potentials for Si(111) at 293K.

Customary expansions of $\bar{U}_0(x)$ employ the Fourier coefficients U_G (Eq. (5.7)) as parameters, and 10 or even 20 terms are often required to obtain the degree of convergence and smoothness shown on Figures 24 and 25. The semiclassical reconstruction method obtains the same accuracy with only one or two terms by choosing the A_m in Eq. (7.12) as the expansion coefficients; this works well because ψ and not x is the "natural" semiclassical variable, and $f(\psi)$ is the function most intimately connected with the critical voltage effect.

8 CONCLUSIONS

The semiclassical method is a series of approximations making use of path concepts from classical mechanics and elementary notions of phase, reflection and interference from wave theory. Applied to diffraction contrast electron microscopy, we have found that even the crudest model with no wave effects included (Sections 2–4) explains much of the structure of "bend contours" observed on micrographs. The important classical concept which we required was the *caustic*, or locus of infinite path density. By allowing the paths to interfere with a phase proportional to their classical action, more features of micrographs could be explained. In

the case of "systematic" diffraction from a set of atomic planes, good quantitative agreement with experiment was obtained (Table I).

By considering the reflections and transmissions of "semiclassical waves" among an array of potential barriers, the nature of the Bloch eigenvalues and eigenvectors in the crystal was clarified (Section 5) and we find good agreement with "exact" determinantal methods (Figure 20). The transition from an "eigenfunction series" to a "classical path series" was seen to be an effect of simple interference among the Bloch waves.

If the effects of inelastic scattering are included in the customary way by making the crystal potential complex (Section 6) the semiclassical method enables predictions to be easily made of which Bloch waves will be absorbed, and which "anomalously transmitted" (Figure 21). As by-products, we obtain a simple and accurate method of predicting the electron energies giving maximum penetration, and an interpretation of the imaginary part of the potential as a classical local inverse mean free path for inelastic scattering.

Finally (Section 7), a more subtle application of interference concepts (still between "semiclassical waves") enabled very accurate predictions to be made (Table II) of the "critical voltages" for which two adjacent sheets of the dispersion surface touch. The analysis suggested an accurate reconstruction method for the projected potential, using measurements of just two numbers (Figures 24, 25).

A theme running throughout our work has been the almost exclusive use of analysis in *real space*. This represents a major departure from conventional practice in electron microscopy, which employs notions from Fourier analysis and reciprocal space.

Where do we go from here? Apart from tying up loose ends, such as the details of the "cross grating" case (Section 4), there are two major areas where further work is required to complete the semiclassical analysis.

First, more methods of *reconstructing the crystal potential* should be developed and tested, to augment the method described in Section 7 based on the critical voltage effect. If the projected potentials $\bar{U}(R)$ can be reconstructed for a number of projection directions involving lattice planes and/or strings, it is easy to get the full three-dimensional potential $V(\mathbf{r})$ with a known accuracy. Then the specimen charge density can be found simply as $\nabla^2 V(\mathbf{r})/4\pi$.

Second, the effects of *departures from perfect lattice symmetry* should be studied. These include the angular distribution of the diffuse fan of electrons resulting from *inelastic scattering*, the images of *lattice defects* such as vacancies and dislocations, and the images of amorphous materials. Of course, each of these subjects has a large literature, but analyses of the quantum-to-classical transition are lacking.

ACKNOWLEDGEMENTS

We are very grateful to Dr. J. W. Steeds for introducing us to this problem and for his constant encouragement, and we thank Dr. P. A. Doyle, Dr. A. C. Enfield and Mr. G. J. Tatlock for many helpful discussions. This work was carried out while one of us (B.F.B.) held an SRC research studentship.

REFERENCES

1. A. Howie, *Phil. Mag.* **14**, 223 (1966); A. Howie, Conf. on Solid St. Physics with Accelerators (Brookhaven Nat. Labs. Rep. BNL 50083-(-52) (1967).
2. L. T. Chadderton, *J. Appl. Cryst.* **3**, 429 (1970).
3. P. B. Hirsch, A. Howie, R. B. Nicholson, D. W. Pashley and M. J. Whelan, *Electron Microscopy of Thin Crystals* (Butterworths, London, 1965).
4. J. Lindhard *Mat. Fys. Medd. Dan. Vid. Selsk* **34**, 1 (1965); M. W. Thompson, *Contemp. Phys.* **9**, 375 (1968).

4a. P. Lervig, J. Lindhard and V. Nielsen, *Nucl. Phys.* **A96**, 481 (1967).

5. Ref. 1 of the test: M. V. Berry, *J. Phys. C.* **4**, 697 (1971).
6. Ref. 2 of the text: M. V. Berry and K. E. Mount, *Reps. Prog. Phys.* **35**, 315 (1972).
7. J. L. Synge, *Encyd. Phys.* (Springer, Berlin, 1960), vol. 3/1.
8. O. N. Stavroudis, *The optics of rays, wavefronts and caustics* (Academic Press, New York, 1972), p. 79.
9. C. J. Richards and J. W. Steeds, *Proc. 25th Anniv. Mtg. EMAG* (Inst. of Phys., London, 1971), p. 128.
10. J. G. Taylor, *Quantum Mechanics: an Introduction* (Allen and Unwin, London, 1970), p. 97.
11. N. Fröman and P. O. Fröman, *JWKB approximation, contributions to the theory* (North-Holland, Amsterdam: 1965).
12. J. M. Ziman, *Solid State Physics* **26**, 1 (sec. 12) (1971).
13. H. Yoshioka, *J. Phys. Soc. Jap.* **12**, 618 (1957).
14. G. Radi, *Z. Phys.* **212**, 146 (1968).
15. P. A. Doyle and M. V. Berry, to appear in Borrmann festschrift edition of *Z. f. Naturforsch* (1973).
16. G. Borrmann, *Phys. Z.* **42**, 157 (1941), G. Borrmann, *Z. Phys.* **127**, 297 (1950).
17. C. J. Humphreys, *Phil. Mag.* **25**, 1459 (1972).
18. J. S. Lally, C. J. Humphreys, A. J. F. Metherell and R. M. Fisher, *Phil. Mag.* **25**, 321 (1972).
19. M. V. Berry and B. F. Buxton, *J. Phys.* to be published.
20. N. F. Mott and H. S. W. Massey, *Theory of Atomic Collisions* (University Press, Oxford, 1965).
21. J. W. Steeds and A. C. Enfield, *Proc. 25th Anniv. Mtg. EMAG* (Institute of Physics, London, 1971) p. 126.
22. R. Landauer, *Phys. Rev.* **82**, 80 (1951).
23. M. S. Spring and J. W. Steeds, *Phys. Stat. Sol.* **37**, 303 (1970), J. W. Steeds, *Phys. Stat. Sol.* **38**, 203 (1971).
24. L. Hewat and C. J. Humphreys, Private Communication.
25. J. W. Steeds, Private communication.
26. J. L. Lebowitz and O. Penrose, *Physics Today* **26**, 23 (1973).